Journal of Power Sources 389 (2018) 198–213

Contents lists available at ScienceDirect

Journal of Power Sources

journal homepage: www.elsevier.com/locate/jpowsour

Review on solid electrolytes for all-solid-state lithium-ion batteries

Feng Zheng[a], Masashi Kotobuki[a,b], Shufeng Song[a,c], Man On Lai[a], Li Lu[a,b,*]

[a] Department of Mechanical Engineering, National University of Singapore, 9 Engineering Drive 1, 117575, Singapore
[b] National University of Singapore, Suzhou Research Institute, Suzhou, 215123, PR China
[c] College of Aerospace Engineering, Chongqing University, Chongqing, 400044, PR China

HIGHLIGHTS

- Focus on solid-state lithium-ion batteries as future energy storage devices.
- Address key component of ion conductors for solid-state battery.
- Introduce advantages of different types of ion conductors.
- Discuss effects of dopants on ionic conductivity in detail.
- Engineer tailored interface to reduce interfacial impedance.

ARTICLE INFO

Keywords:
Lithium-ion battery
Solid electrolyte
Electrochemical property

ABSTRACT

All-solid-state (ASS) lithium-ion battery has attracted great attention due to its high safety and increased energy density. One of key components in the ASS battery (ASSB) is solid electrolyte that determines performance of the ASSB. Many types of solid electrolytes have been investigated in great detail in the past years, including NASICON-type, garnet-type, perovskite-type, LISICON-type, LiPON-type, Li_3N-type, sulfide-type, argyrodite-type, anti-perovskite-type and many more. This paper aims to provide comprehensive reviews on some typical types of key solid electrolytes and some ASSBs, and on gaps that should be resolved.

1. Introduction of traditional and all-solid-state lithium-ion batteries

Lithium-ion batteries have achieved great market share since their commercialization by Sony in 1990. Compared with other energy storage devices, lithium-ion batteries have demonstrated a lot of advantages, including high energy density, long cycle life etc [1]. Currently, lithium-ion batteries have been used in many products, such as consumer electronics, electric/hybrid electric vehicles, stationary energy storage systems etc.

However, traditional lithium-ion batteries have critical safety issues because of use of highly flammable organic liquid electrolytes or polymer electrolytes which have low thermal stability and low flame point so that it is easy to cause fire accidents and explosion if they are improperly used [2,3]. To thoroughly address the safety issues, use of highly flammable organic liquid electrolytes should be entirely avoided as such all-solid-state batteries (ASSBs) become a good choice because the organic liquid electrolytes are replaced by inorganic solid electrolytes that have high thermal stability. At the same time, ASSBs also have many other advantages [4,5]. Firstly, as no liquid electrolyte is used, packaging for ASSBs can be much simplified so that dead weight in battery packaging can be largely reduced, resulting in increased energy density. Secondly, compared with organic liquid electrolytes and polymer electrolytes, inorganic solid electrolytes have much better electrochemical stability and are compatible with higher potential cathode materials to increase energy density. Thirdly, ASSBs have excellent mechanical properties.

Organic liquid electrolyte and separator in the traditional battery are replaced by inorganic solid electrolyte in the ASSB, which is the main difference [5,6]. Working principles of these two types of batteries are the same. During charging, Li-ions deintercalate from cathode and transport through electrolyte and electrolyte-electrode interfaces into anode, and electrons move from cathode to anode through external circuit. During discharging, movement of Li-ions and electrons are reversibly reversed. Main functions of solid electrolytes are the same as liquid electrolytes and separators that only allow Li-ions to crossover between cathode and anode, and prevent electron conduction and short-circuit. Thus, several basic requirements for solid electrolytes are essential. Electrolytes should

* Corresponding author. Department of Mechanical Engineering, National University of Singapore, 9 Engineering Drive 1, 117575, Singapore.
E-mail address: luli@nus.edu.sg (L. Lu).

https://doi.org/10.1016/j.jpowsour.2018.04.022
Received 1 February 2018; Received in revised form 3 April 2018; Accepted 5 April 2018
Available online 12 April 2018
0378-7753/

- possess high ionic conductivity of above 10^{-4} S cm^{-1} at room temperature,
- have negligible electronic conductivity with a high ionic transference number, and
- have wide electrochemical stability windows [7].

2. Selective review of solid electrolytes of all-solid-state lithium-ion batteries

Several types of Li-ion solid electrolytes can provide above needs, including NASICON, garnet, perovskite, LISICON, LiPON, Li_3N, sulfide, argyrodite, anti-perovskite etc [8–11]. The advantages and future improvements of these solid electrolytes are discussed in this section.

2.1. NASICON-type electrolytes

The name of NASICON was initiated from sodium super ion conductor with formula $NaM_2(PO_4)_3$ where M is cation and one of examples is $Na_{1+x}Zr_2Si_xP_{3-x}O_{12}$ ($0 \le x \le 3$) [12,13]. This type of solid electrolyte has a rhombohedral structure with space group of R-3c, except for the range $1.8 \le x \le 2.2$, where the structure exhibits a small distortion to monoclinic space group of C2/c [13]. The rhombohedral structure is shown in Fig. 1 [14] where XO_4 (PO_4 or SiO_4) tetrahedrons and MO_6 (ZrO_6) octahedrons are connected to each other to form a 3D framework and pathways for ion diffusion, and oxygen-ions are shared by the tetrahedrons and octahedrons. Mobile ions (Na-ions) occupy A sites and diffuse along c-axis by jumping between A1 (6b) and A2 (18e) sites. Monoclinic distortion could lead to separation of A2 (18e) sites in the rhombohedral structure (R-3c, Z = 6) into 4e and 8f sites in the monoclinic structure (C2/c, Z = 4) [13,15]. When x = 0, only A1 sites are occupied, each of which is octahedrally coordinated by six oxygen-ions from two neighboring MO_6 octahedrons. In this case, activation energy for transport of mobile ions is high because of inequality of site-preference energies of A1 and A2 sites. When $x > 0$, partial A2 sites are occupied by extra mobile ions, and activation energy is decreased due to electrostatic interaction between mobile ions [13]. At the same time, the diffusion is restricted by size of bottlenecks along the pathways, which is determined by the framework ions. Diameter of the narrowest bottleneck should be larger than twice the sum of radii of mobile ion and oxygen-ion [13]. Thus, it is important to choose appropriate framework ions according to mobile ion's radius to benefit ion diffusion and improve ionic conductivity. Goodenough et al. [15] demonstrated that NASICON $Na_3Zr_2PSi_2O_{12}$ with monoclinic structure showed ionic conductivity of 2×10^{-1} S cm^{-1} at 300 °C, which is comparable to β"-alumina, an excellent Na-ion conductor. Furthermore, Na-ion in $Na_3Zr_2PSi_2O_{12}$ could conduct in three dimensions, addressing the problem of 2-dimensional conduction of β"-alumina.

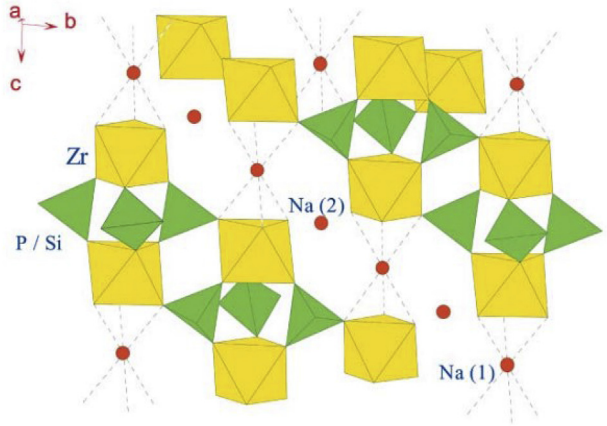

Fig. 1. Crystal structure of NASICON-type solid electrolytes. Reproduced from Ref. [14] with permission of The Royal Society of Chemistry.

NASICON-type Li-ion solid electrolyte $LiZr_2(PO_4)_3$ can be prepared by replacing Na-ion in $NaZr_2(PO_4)_3$ by Li-ion. However, $LiZr_2(PO_4)_3$ showed much lower ionic conductivity than that of $NaZr_2(PO_4)_3$ [16]. $LiZr_2(PO_4)_3$ prepared at 1200 °C (named as high temperature phase, because prepared at high temperature) showed a NASICON-type monoclinic structure with space group of Cc and ionic conductivity of 3.3×10^{-6} S cm^{-1} at room temperature. The high temperature phase exhibited a phase transition from monoclinic (Cc) to rhombohedral (R-3c) when heated to about 40 °C, leading to a high conducting phase with ionic conductivity of 1.2×10^{-2} S cm^{-1} at 300 °C. $LiZr_2(PO_4)_3$ prepared at 900 °C (named as low temperature phase, because prepared at low temperature) showed a β-$Fe_2(SO_4)_3$-type monoclinic structure with space group of $P2_1/n$ and ionic conductivity of 10^{-10} S cm^{-1} at room temperature. The low temperature phase also exhibited a phase transition from monoclinic ($P2_1/n$) to orthorhombic (probably Pcan) when heated to 300 °C, leading to a high conducting phase with ionic conductivity of 5×10^{-4} S cm^{-1} at 300 °C. Aono et al. [17] studied NASICON-type $LiM_2(PO_4)_3$ (M = Ge, Ti, Hf), and found that $LiTi_2(PO_4)_3$ showed the minimum activation energy and the highest ionic conductivity. Among the NASICON-type electrolytes, skeleton of $LiTi_2(PO_4)_3$ was the most suitable one for Li-ion diffusion; however, its conductivity was still low because of low sinterability. By partially replacing M^{4+} ions by trivalent ions, $Li_{1+x}Al_xGe_{2-x}(PO_4)_3$, $Li_{1+x}Al_xTi_{2-x}(PO_4)_3$ and $Li_{1+x}Fe_xHf_{2-x}(PO_4)_3$ were obtained with low porosities and enhanced ionic conductivities of higher than 10^{-4} S cm^{-1} at 25 °C. $Li_{1.3}Al_{0.3}Ti_{1.7}(PO_4)_3$ revealed the highest ionic conductivity of 7×10^{-4} S cm^{-1} at 25 °C, which is comparable to other high Li-ion conducting materials. However, Ti^{4+} in $Li_{1+x}Al_xTi_{2-x}(PO_4)_3$ could be reduced by lithium, thus, $Li_{1+x}Al_xGe_{2-x}(PO_4)_3$ and $Li_{1+x}Fe_xHf_{2-x}(PO_4)_3$ are more promising because of their excellent stability. By adding Li_3PO_4 or Li_3BO_3 to $LiTi_2(PO_4)_3$, dense electrolytes could be obtained, and high ionic conductivity of 3×10^{-4} S cm^{-1} at 25 °C was achieved for $LiTi_2(PO_4)_3$-0.2Li_3BO_3 because of enhanced grain boundary ionic conductivity and contact between grains [18]. With increase in lithium-salt addition, activation energy of bulk ionic conductivity remained constant, while that of grain boundary ionic conductivity was noted to decrease. Both bulk and grain boundary ionic conductivities were enhanced by lithium-salt addition. The enhancement of grain boundary ionic conductivity was due to decrease of porosity and activation energy, which in turn increased bulk ionic conductivity since bulk ionic conductivity is dependent on grain boundary ionic conductivity. Substitution of Ti^{4+} in $LiTi_2(PO_4)_3$ by trivalent elements was studied in detail [19–21]. For $Li_{1+x}M_xTi_{2-x}(PO_4)_3$ (M = Al, Sc, Y, La), ionic conductivities of electrolytes were observed to increase with increase in Li concentration until x = 0.3, and the mechanism of the increase in ionic conductivity should be attributed to increased Li-ion concentration and decreased porosity [19]. For $Li_{1+x}M_xTi_{2-x}(PO_4)_3$ with M to be Al, Cr, Ga, Fe, Sc, In, a single phase could be obtained, while for M to be Lu, Y, La, mixed phases of $LiTi_2(PO_4)_3$ and $Li_3M_2(PO_4)_3$ were obtained [20,21]. For all M^{3+} substituted $Li_{1+x}M_xTi_{2-x}(PO_4)_3$, porosity was decreased, and Cr^{3+} substituted electrolyte showed the highest porosity, close to that of $LiTi_2(PO_4)_3$ (34%). It was assumed that the substitution could cause formation of some glassy second phase which increased density. While Cr^{3+} has close ionic radius with Ti^{4+}, Ti^{4+} could be replaced by Cr^{3+} easily, and no more Cr^{3+} could help form glassy second phase at grain boundaries. Ionic conductivity of $Li_{1+x}M_xTi_{2-x}(PO_4)_3$ has been observed to increase with increase in M^{3+} substitution, even for the ones with mixed phases (M = Lu, Y, La). This was due mainly to densification of electrolytes, and the highest ionic conductivity of 7×10^{-4} S cm^{-1} at 25 °C was obtained for $Li_{1.3}M_{0.3}Ti_{1.7}(PO_4)_3$ (M = Al, Sc). Fu et al. [22] used melt-quench method to prepare glass-ceramic solid electrolytes 2[$Li_{1+x}Ti_2Si_xP_{3-x}O_{12}$]-$AlPO_4$. Lattice parameters of major conductive phase (based on $LiTi_2P_3O_{12}$) increased with Si concentration until x = 0.1 due to substitution of P^{5+} by Si^{4+}, followed by decreased when x was further

increased from 0.1 to 0.4, which was due to substitution of Ti^{4+} by Al^{3+}. For $x > 0.4$, the lattice parameters remained almost unchanged, probably because the substitutions reached saturation. For x = 0.4, the maximum ionic conductivity of 1.5×10^{-3} S cm^{-1} at room temperature was obtained, which meets the requirement for application in ASSBs. By melt-quench method, Goharian et al. [23] prepared glass-ceramics in 100 part [$Li_{1+x}Cr_xTi_{2-x}(PO_4)_3$] and 5 part SiO_2 system, and the one with x = 0.5 attained extremely high ionic conductivity of 2.14×10^{-2} S cm^{-1} at 25 °C. With x increased from 0 to 0.5, Cr^{3+} was incorporated into $LiTi_2(PO_4)_3$ to substitute Ti^{4+}, and crystallinity of the NASICON increased with decrease of TiO_2 impurity. The x = 0.5 glass-ceramic also showed tight contact between grains that could lead to high grain boundary ionic conductivity. These effects together with increased Li-ion amount led to the high ionic conductivity. However, Eckert et al. [24] reported that this high ionic conductivity in Ref. [23] could not be reproduced, thus, this needs further examination.

Although $Li_{1+x}Al_xTi_{2-x}(PO_4)_3$ (LATP) showed high ionic conductivity, it suffered a redox reaction at 2.5 V vs. Li/Li^+ because of reduction of Ti^{4+}, making it incompatible with many low potential anode materials, including lithium [25–27]. Reduction of LATP by lithium or C_6Li may induce electronic conductivity in solid electrolyte and cause short-circuit for battery [25]. Li insertion into $LiTi_2(PO_4)_3$ was conducted [26]. Intercalation and deintercalation could process reversibly, and two solid solutions $Li_{1+x}Ti_2(PO_4)_3$ ($0 \le x \le 0.23$ and $1.72 \le x \le 2$) were found separated by a two-phase domain ($0.23 \le x \le 1.72$). Both the end products $LiTi_2(PO_4)_3$ and $Li_3Ti_2(PO_4)_3$ exhibited rhombohedral NASICON structures, but lithium distributions were different in these two structures. In $LiTi_2(PO_4)_3$, Li-ions fully occupied A1 (6b, Z = 6) sites with empty A2 (18e, Z = 6) sites, while in $Li_3Ti_2(PO_4)_3$ A2 (18e, Z = 6) sites were fully occupied with empty A1 (6b, Z = 6) sites. This peculiar lithium distribution in $Li_3Ti_2(PO_4)_3$ increased repulsion between neighboring TiO_6 octahedrons and extended c axis. Structure of $Li_3Ti_2(PO_4)_3$ was further studied by X-ray diffraction, neutron diffraction and ^{7}Li MAS NMR, and it was found that Li-ions occupied two subsites in the A2 (18e, Z = 6) cavities [27].

Another kind of NASICON-type solid electrolyte is $Li_{1+x}Al_xGe_{2-x}(PO_4)_3$ (LAGP), showing high ionic conductivity of above 10^{-4} S cm^{-1} at room temperature [28,29]. LAGP glass-ceramics were prepared by melt-quench and recrystallization [28]. Ionic conductivity reached the maximum value of 4.0×10^{-4} S cm^{-1} at room temperature for x = 0.5, which is higher than LAGP prepared by conventional sintering. Crystalline in glass-ceramic form could have dense microstructure and close contact between grains, which is the main reason for the enhancement of ionic conductivity. Based on $Li_{1.5}Al_{0.5}Ge_{1.5}(PO_4)_3$ glass-ceramic, excess Li_2O was added to prepare $Li_{1.5}Al_{0.5}Ge_{1.5}(PO_4)_3$-x$Li_2O$ glass-ceramics [29]. It was believed that some excess lithium was incorporated into crystal lattice of $Li_{1.5}Al_{0.5}Ge_{1.5}(PO_4)_3$, and secondary lithium-containing phases were formed from excess lithium, which could act as nucleating agents for crystallization of glasses. $Li_{1.5}Al_{0.5}Ge_{1.5}(PO_4)_3-0.05Li_2O$ reached the maximum ionic conductivity with bulk and total values of 1.18×10^{-3} S cm^{-1} and 7.25×10^{-4} S cm^{-1} at room temperature, respectively. This composition showed excellent electrochemical stability with lithium deposition and dissolution at voltage between 0.5 V and 0.4 V vs. Li/Li^+ and was stable up to 6 V vs. Li/Li^+. Thokchom et al. [30] prepared glass-ceramic with composition of 19.75 Li_2O·6.17 Al_2O_3·37.04 GeO_2·37.04 P_2O_5 by melt-quench and crystallization. The one crystallized at 850 °C for 12 h showed the highest ionic conductivity of 5.08×10^{-3} S cm^{-1} at 27 °C, and the superionic conducting phase was $Li_{1.5}Al_{0.5}Ge_{1.5}(PO_4)_3$. Higher crystallization temperature (950 °C) led to dielectric impurity phase $AlPO_4$, which could interact with Li^+ to form space charge that mediated ion transport and caused higher activation energy. Simultaneous doping of Ge by Al and Cr in $LiGe_2(PO_4)_3$ was investigated with designed compositions of $Li_{1+x+y}Al_xCr_yGe_{2-x-y}(PO_4)_3$ (x + y = 0.5) [31]. The samples with y = 0, 0.1, 0.25, 0.4 and 0.5 showed main phases related to NASICON $LiGe_2(PO_4)_3$, and the one with y = 0.1 contained no secondary $CrPO_4$ phase and the least amount of GeO_2. Accordingly, $Li_{1.5}Al_{0.4}Cr_{0.1}Ge_{1.5}(PO_4)_3$ demonstrated the highest ionic conductivity of 6.65×10^{-3} S cm^{-1} at 26 °C. Thus, proper amount of Cr doping could induce high ionic conductivity of $LiGe_2(PO_4)_3$ glass-ceramic. Furthermore, $Li_{1.5}Al_{0.4}Cr_{0.1}Ge_{1.5}(PO_4)_3$ exhibited lithium deposition and dissolution at voltage between − 0.53 V and 0.44 V vs. Li/Li^+ and was stable up to 7 V vs. Li/Li^+. Kunshina et al. [32] developed a liquid-phase method to synthesize $Li_{1.5}Al_{0.5}Ge_{1.5}(PO_4)_3$ solid electrolyte. Compared with solid-phase method, the liquid-phase method could obtain GeO_2 existed in highly active amorphous state, which could decrease temperature and duration of synthesis. A single-phase $Li_{1.5}Al_{0.5}Ge_{1.5}(PO_4)_3$ solid electrolyte could be obtained by the liquid-phase method, which showed higher conductivity than the counterpart prepared by solid-phase method. A cold sintering process (CSP) was reported to densify $Li_{1.5}Al_{0.4}Cr_{0.1}Ge_{1.5}(PO_4)_3$ electrolytes at low temperatures, which could avoid lithium loss and second phase formation caused by high-temperature heat treatments [33]. Through CSP at 120 °C for 20 min, relative density of the electrolyte reached 80%, and further heat treatment at 650 °C for 5 min led to ionic conductivity of 5.4×10^{-5} S cm^{-1} at 25 °C.

Feng et al. [34] reported an electrochemical stability window of $Li_{1.5}Al_{0.5}Ge_{1.5}(PO_4)_3$ to be 0.85–7 V vs. Li/Li^+, and mechanism of reduction of the electrolyte at low potential vs. Li/Li^+ was assumed to be:

$$Li_{1.5}Al_{0.5}Ge_{1.5}(PO_4)_3 + 6\ Li^+ + 6\ e^- \rightarrow 1.5\ Ge + 2.5\ Li_3PO_4 + 0.5\ AlPO_4 \quad (1)$$

$$1.5\ Ge + 6.6\ Li^+ + 6.6\ e^- \rightarrow 1.5\ Li_{4.4}Ge \quad (2)$$

Reversible deposition and dissolution of lithium were observed at voltage between − 0.8 V and 0.8 V vs. Li/Li^+, indicating that $Li_{1.5}Al_{0.5}Ge_{1.5}(PO_4)_3$ maintained Li-ion conducting property though being reduced by lithium. $Li_{1.5}Al_{0.5}Ge_{1.5}(PO_4)_3$ was tested as anode material and showed good retention with reversible capacity of 300 mAh g^{-1} at 150 mA g^{-1} for 100 cycles and coulombic efficiency of almost 100%. It was presumed that Li_3PO_4 and $AlPO_4$ produced during reduction of $Li_{1.5}Al_{0.5}Ge_{1.5}(PO_4)_3$ surrounded Ge, which could buffer volume change of Ge during alloying and de-alloying with lithium. Excellent rate performance was also obtained for $Li_{1.5}Al_{0.5}Ge_{1.5}(PO_4)_3$, which showed capacity of about 180 mAh g^{-1} at current of 1500 mA g^{-1}. However, the reversible charge-discharge only happened for reaction (2), and it is not clear yet whether reaction (1) could also process reversibly.

LAGP is a very promising solid electrolyte for applications in ASSBs. However, GeO_2, one of precursors for preparation of LAGP, is expensive, which can significantly increase cost of LAGP-based ASSBs [35]. Thus, it is important to replace Ge with other cheaper elements, which at the same time may also reduce ionic conductivity. Balance between the property and the cost should be considered for application of LAGP in ASSBs.

2.2. Garnet-type electrolytes

Lithium-containing garnets were firstly discovered in 1968 with composition of $Li_3Ln_3M_2O_{12}$ (M = Te, W; Ln = Y, Pr, Nd, Sm, Eu, Gd, Tb, Dy, Ho, Er, Tm, Yb, Lu) [36]. For $Li_3Ln_3Te_2O_{12}$, lattice constant is greatly influenced by ionic radius of Ln element, compared with garnet $Ln_3Ga_5O_{12}$. $Li_3Ln_3Te_2O_{12}$ could form garnets with more types of Ln elements than $Li_3Ln_3W_2O_{12}$, which was due possibly to relatively stable regular TeO_6 octahedrons formed inside $Li_3Ln_3Te_2O_{12}$ garnets, while for $Li_3Ln_3W_2O_{12}$ distorted WO_6 octahedrons formed. Thangadurai et al. [37] firstly reported the garnet, $Li_5La_3M_2O_{12}$ (M = Ta, Nb), showing lithium ionic conductivities in the magnitude of 10^{-6} S cm^{-1} at 25 °C. $Li_5La_3Nb_2O_{12}$ showed slightly higher ionic conductivity and lower activation energy than $Li_5La_3Ta_2O_{12}$. These compounds were isotropic conductors, and Li-ions could diffuse in the 3-dimensional framework. At the same time, $Li_5La_3Ta_2O_{12}$ was found to be stable in contact with

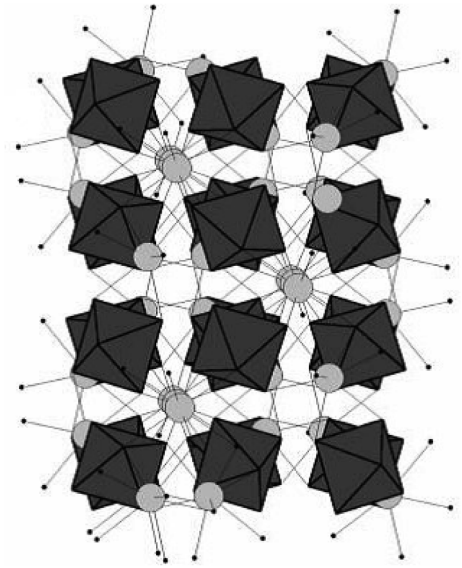

Fig. 2. Framework of garnet-type solid electrolytes $Li_5La_3M_2O_{12}$ (M = Ta, Nb). Reproduced from Ref. [39] with permission of The Royal Society of Chemistry.

molten lithium, which was probably because Ta is less reducible than other transition metals including Ti, Nb etc. Doping strategy has also been used to modify the garnets. For instance, Ba-doped $Li_6BaLa_2Ta_2O_{12}$ showed ionic conductivity of 4.0×10^{-5} S cm^{-1} at 22 °C [38]. For $Li_6BaLa_2Ta_2O_{12}$ and $Li_6SrLa_2Ta_2O_{12}$, total ionic conductivities showed the same magnitude as bulk ionic conductivities, and they are superior to other types of oxide electrolytes. $Li_6BaLa_2Ta_2O_{12}$ was found to be stable against molten lithium as well, and to be stable up to 6 V vs. Li/Li$^+$, exhibiting excellent electrochemical stability. Nb-doped $Li_6BaLa_2Nb_2O_{12}$ showed dark color after contact with molten lithium, indicating reduction of the electrolyte. Thus, Ta is an important transition metal element to enhance electrochemical stability of oxide solid electrolyte. Crystal structure of $Li_5La_3M_2O_{12}$ (M = Ta, Nb) is cubic with a space group of Ia-3d (#230). Its framework is composed of La, M and O ions, and Li-ions distribute inside the framework, as shown in Fig. 2 [39]. For $Li_5La_3Ta_2O_{12}$, Li-ions occupy 24d sites inside tetrahedrons with occupancy of 0.802(4), and 48 g and 96 h sites inside octahedrons with occupancies of 0.139(8) and 0.147(9), respectively. Thus, occupancy of Li-ions inside octahedrons is 0.433(1), and 67.9% of the octahedral Li-ions are displaced. The octahedrons are connected by shared edges, and distances between Li-ions in neighbouring octahedrons are irregular due to the displacement of Li-ions. The shortest separation between Li-ions can lead to facile Li-ion hopping and high ionic conductivity. $Li_5La_3Nb_2O_{12}$ shows similar structure and Li-ion occupancies as $Li_5La_3Ta_2O_{12}$, thus, ionic conduction in $Li_5La_3Nb_2O_{12}$ should originate from the same mechanism as $Li_5La_3Ta_2O_{12}$.

Murugan et al. [40] prepared a new garnet-type of solid electrolyte, $Li_7La_3Zr_2O_{12}$ (LLZO), showing ionic conductivity of about 3×10^{-4} S cm^{-1} at 25 °C, and its crystal structure was cubic, the same as that of $Li_5La_3M_2O_{12}$ (M = Ta, Nb) [39]. Grain boundary resistance was found to be less than 50% of total resistance, thus, total ionic conductivity was in the same magnitude as bulk ionic conductivity, leading to high total ionic conductivity. Geiger et al. [41] discovered that $Li_7La_3Zr_2O_{12}$ underwent a phase transition from tetragonal to cubic at 100–150 °C, and the cubic phase exhibited higher ionic conductivity than the tetragonal phase. Therefore, stabilization of cubic phase at room temperature becomes critical. It was noted experimentally that a cubic phase could be achieved when $Li_7La_3Zr_2O_{12}$ was sintered in an alumina crucible [41]. Detailed studies showed that Al^{3+} doping in Li^+ sites could stabilize the high temperature cubic phase to room temperature. Ohta et al. [42] partially doped Nb^{5+} on Zr^{4+} sites to obtain $Li_{6.75}La_3(Zr_{1.75}Nb_{0.25})O_{12}$, resulting in an ionic conductivity of 8×10^{-4} S cm^{-1} at 25 °C and a wide electrochemical stability window of 0–9 V vs. Li/Li$^+$. Bulk resistance contributed to main part of total resistance, and variation of ionic conductivity upon variation of Nb doping amount was presumed to be due to change of Li-ion mobility inside grains. An ASSB was constructed using $Li_{6.75}La_3(Zr_{1.75}Nb_{0.25})O_{12}$ as solid electrolyte with lithium as anode and PLD prepared $LiCoO_2$ as cathode, which realized charge-discharge capacities of about 90% of theoretical capacity, demonstrating that $Li_{6.75}La_3(Zr_{1.75}Nb_{0.25})O_{12}$ was appropriate for application in ASSBs. Murugan et al. [43] used Y^{3+} to dope Zr^{4+} site in $Li_7La_3Zr_2O_{12}$, and the obtained $Li_{7.06}La_3Y_{0.06}Zr_{1.94}O_{12}$ showed high bulk and total ionic conductivities of 9.56×10^{-4} S cm^{-1} and 8.10×10^{-4} S cm^{-1} at 25 °C, respectively, which were higher than those of $Li_7La_3Zr_2O_{12}$. One of the key requirements to achieve high total conductivity is to obtain a dense microstructure so that the grain boundary conductivity can be largely increased. Li et al. [44] prepared $Li_{7-x}La_3Zr_{2-x}Ta_xO_{12}$ for x = 0.6 by solid-state reaction in alumina crucibles, and achieved ionic conductivity of 1.0×10^{-3} S cm^{-1} at room temperature. The prepared $Li_{6.4}La_3Zr_{1.4}Ta_{0.6}O_{12}$ was electrochemically stable at voltage between 0 and 5 V vs. Li/Li$^+$. Certain amount of Al element was detected in grain boundaries of the pellet. Al was obviously from alumina crucible and acted as sintering aid to induce a good bonding between grains and hence promoted Li-ion conduction in the grain boundaries. Ga-substituted $Li_{6.55}Ga_{0.15}La_3Zr_2O_{12}$ was prepared in a dried O_2 atmosphere, and showed ionic conductivity of 1.3×10^{-3} S cm^{-1} at 24 °C and 2.2×10^{-3} S cm^{-1} at 42 °C [45]. Ga atoms located in tetrahedral positions, which could promote random distribution of Li-ions and increased ionic conductivity. However, when the amount of Ga is higher than 0.15, Li-ions transportation in the tetrahedral positions could be blocked, leading to a decrease in ionic conductivity. The dry sintering atmosphere could avoid Li$^+$/H$^+$ exchange due to moisture, while $Li_{7-3x}Ga_xLa_3Zr_2O_{12}$ (x = 0, 0.15, 0.2, 0.3) prepared in the ambient atmosphere showed relative density of lower than 70% and $Li_{6.4}Ga_{0.2}La_3Zr_2O_{12}$ showed ionic conductivity of 1.5×10^{-6} S cm^{-1} at 24 °C, which was about three magnitudes lower than that of the counterpart prepared in dry atmosphere. Rettenwander et al. [46] co-substituted Al and Ga in $Li_7La_3Zr_2O_{12}$ to prepare $Li_{6.4}Al_{0.2-x}Ga_xLa_3Zr_2O_{12}$ ($0 \le x \le 0.2$). Structures of the electrolytes showed phase transition from garnet space group of Ia-3d (x = 0.00, 0.05, 0.10) to non-garnet space group of I-43d (x = 0.15, 0.20). This phase transition led to decrease of activation energy from ~0.28 eV (x = 0.05, 0.10) to ~0.26 eV (x = 0.15, 0.20) and increase of ionic conductivity from 2.63×10^{-4} S cm^{-1} (x = 0.00) to 1.18×10^{-3} S cm^{-1} (x = 0.20) at 20 °C. The one of x = 0.20 tested with Li electrodes showed ionic conductivity of 1.32×10^{-3} S cm^{-1} at 20 °C. Wu et al. [47] investigated influence of Ga doping on $Li_{7-3x}Ga_xLa_3Zr_2O_{12}$. For $x < 0.20$, the garnets showed both cubic and tetragonal structures, while for $x \ge 0.20$, there existed only cubic structure, which showed higher ionic conductivity. $Li_{6.25}Ga_{0.25}La_3Zr_2O_{12}$ (x = 0.25) showed the highest ionic conductivity of 1.46×10^{-3} S cm^{-1} at 25 °C. Buannic et al. [48] prepared $Li_{6.55+y}Ga_{0.15}La_3Zr_{2-y}Sc_yO_{12}$ by a dual substitution strategy. The Ga substitution could stabilize cubic crystal structure, and the Sc substitution could increase Li-ion number. $Li_{6.65}Ga_{0.15}La_3Zr_{1.90}Sc_{0.10}O_{12}$ (y = 0.10) showed the highest ionic conductivity of 1.8×10^{-3} S cm^{-1} at 27 °C, which was related to Li-only occupation of Li_{96h} sites. Wu et al. [49] doped Rb at La sites in $Li_{6.10}Ga_{0.30}La_3Zr_2O_{12}$, and achieved high ionic conductivity of 1.62×10^{-3} S cm^{-1} at room temperature for $Li_{6.20}Ga_{0.30}La_{2.95}Rb_{0.05}Zr_2O_{12}$. The high ionic conductivity was possibly related to a structural change and a higher Li$^+$ concentration caused by Rb doping.

The gartnet-type of Li-ion conductors is very promising for application in ASSBs. However, it was not stable in the ambient atmosphere due to moisture and CO_2 [50,51]. Thus, it is important to increase stability of LLZO in the ambient atmosphere.

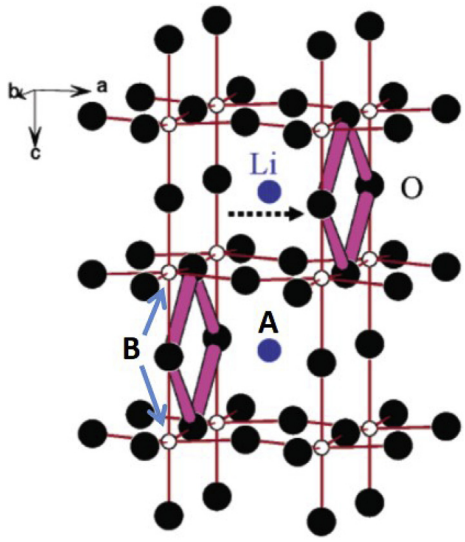

Fig. 3. Crystal structure of perovskite-type solid electrolytes $Li_{3x}La_{2/3-x}TiO_3$. Adapted with permission from Ref. [53]. Copyright (2003) American Chemical Society.

2.3. Perovskite-type electrolytes

Inaguma et al. [52] firstly prepared perovskite-type solid electrolytes $Li_{3x}La_{2/3-x}TiO_3$ (LLTO), which showed bulk ionic conductivity of 1×10^{-3} S cm^{-1} and total ionic conductivity of higher than 2×10^{-5} S cm^{-1} at room temperature for $Li_{0.34(1)}La_{0.51(1)}TiO_{2.94(2)}$. Crystal structure of LLTO is shown in Fig. 3 [53] where Li and La ions occupy centre A sites, and Ti-ions occupy corner B sites. Oxygen-ions form bottlenecks causing potential barriers for Li-ions migration from one A site to a neighboring A site. Since size of the bottlenecks can be changed by changing lattice parameters, many attempts tried to enlarge lattice parameters of the perovskite-type solid electrolytes. Inaguma et al. [54] doped 5 mol% Sr^{2+} in A sites of $Li_{1/2}La_{1/2}TiO_3$, and achieved bulk ionic conductivity of 1.5×10^{-3} S cm^{-1} at 27 °C. Substitution of La and Li by Sr increased lattice constant of perovskite structure, thus, diffusion space of Li-ion was increased and ionic conductivity was improved. However, doping by Sr also caused decrease of Li-ion concentration, and would decrease ionic conductivity when amount of Sr was higher than 0.1. At the same time, research on $Li_{3x}La_{2/3-x}TiO_3$ showed that ionic conductivity was influenced by fractions of Li-ions and vacancies at A sites.

Despite the high bulk ionic conductivity, the grain boundary ionic conductivity of LLTO was only in the magnitude of 10^{-5} S cm^{-1} at room temperature, resulting in low total ionic conductivity [52]. At the same time, LLTO was not stable at voltage below about 1.8 V vs. Li/Li$^+$, making it incompatible with many low potential anode materials, including lithium [55]. The low electrochemical stability was caused by Ti^{4+} in LLTO since it can be reduced at low voltage vs. Li/Li$^+$. Two lithiation steps of 1.8–1.1 V and 0.6–0 V vs. Li/Li$^+$ were observed for $Li_{0.35}La_{0.55}TiO_3$, and the step of 1.8–1.1 V was assigned to lithium insertion into $Li_{0.35}La_{0.55}TiO_3$. About 0.75–0.9 Li could be inserted into $Li_{0.35}La_{0.55}TiO_3$ during the first lithiation step, but amount of reversibly inserted/extracted Li was 0.48. A possible phase transition from ABO_3 perovskite phase to A_2BO_3 monoclinic phase was proposed for $Li_{0.35}La_{0.55}TiO_3$ with 0.24 Li insertion. Thus, it is necessary to substitute Ti by other elements to increase the electrochemical stability.

To address this issue, Chung et al. [56] substituted Ti^{4+} with Sn^{4+}, Zr^{4+}, Mn^{4+} and Ge^{4+}, and found that ionic conductivity was increased by substitution of Mn^{4+} and Ge^{4+}. However, to avoid formation of second phase, only partial Ti^{4+} could be substituted and the remaining Ti^{4+} could still be reduced. Thangadurai et al. [57] synthesized a new perovskite-type solid electrolyte $LiSr_{1.65}Zr_{1.3}Ta_{1.7}O_9$ that was stable in contact with lithium because oxidation states of Zr^{4+} and Ta^{5+} are stable against reduction. However, ionic conductivity of $LiSr_{1.65}Zr_{1.3}Ta_{1.7}O_9$ was as low as 1.3×10^{-5} S cm^{-1} at 30 °C, which is lower than the 10^{-4} S cm^{-1} requirement for solid electrolytes. In order to improve ionic conductivity, Chen et al. [7] further investigated composition $Li_{2x-y}Sr_{1-x}Ta_yZr_{1-y}O_3$ and found that $Li_{3/8}Sr_{7/16}Ta_{3/4}Zr_{1/4}O_3$ (LSTZ) showed the highest ionic conductivity with bulk and grain boundary ones of 2×10^{-4} S cm^{-1} and 1.33×10^{-4} S cm^{-1} at 30 °C, respectively. Though its bulk ionic conductivity is one magnitude lower than that of LLTO, its grain boundary ionic conductivity is one magnitude higher than that of LLTO, leading to better total ionic conductivity. At the same time, LSTZ was stable at voltage above 1.0 V vs. Li/Li$^+$, making it compatible with many low potential anode materials, including $Li_4Ti_5O_{12}$, TiO_2, Nb_2O_5 etc. At voltage below 1 V vs. Li/Li$^+$, about 0.08 Li could be inserted into $LiSr_{1.65}Zr_{1.3}Ta_{1.7}O_9$, which is much lower than 0.48 of $Li_{0.35}La_{0.55}TiO_3$. Inada et al. [58] prepared LSTZ by powder-bed sintering, and the obtained electrolyte showed high ionic conductivity with bulk and total ones of 3.5×10^{-4} S cm^{-1} and 2.7×10^{-4} S cm^{-1} at 27 °C, respectively. Compared with LSTZ sintered without mother powder, LSTZ sintered with mother powder showed less amount of impurities and Li loss during high temperature reaction was largely suppressed. Density and grain size of LSTZ were also improved by powder-bed sintering method. Due to these effects, total conductivity was improved to about 3 times of previously reported value (8×10^{-5} S cm^{-1} at 30 °C). $Li_{2x-y}Sr_{1-x}Ta_yZr_{1-y}O_3$ (x = 0.75y) was further studied in detail [59]. Almost single perovskite LSTZ phase could be obtained for y = 0.60–0.75, and ionic conductivity increased with increase of y. The maximum ionic conductivity with bulk and total ones of 2.8×10^{-4} S cm^{-1} and 2×10^{-4} S cm^{-1} at 27 °C was obtained for $Li_{3/8}Sr_{7/16}Ta_{3/4}Zr_{1/4}O_3$ (y = 0.75). By replacing Zr with Hf, $Li_{3/8}Sr_{7/16}Ta_{3/4}Hf_{1/4}O_3$ (LSTH) was prepared by solid-state reaction [60]. It showed higher ionic conductivity (3.8×10^{-4} S cm^{-1} at 25 °C) than LSTZ. The electrochemical stability window was from 1.4 V to at least 4.5 V vs. Li/Li$^+$.

While LSTZ and LSTH are promising solid electrolyte for ASSBs, there are still some bottleneck issues restricting their applications. Firstly, preparation temperature of LSTZ/LSTH was 1300 °C, which is very harsh and incompatible with electrode materials for battery construction using co-sintering method. To decrease processing temperature, Chen et al. [61] studied $Li_{3/8}Sr_{7/16}Nb_{3/4}Zr_{1/4}O_3$ (LSNZ) electrolyte, and found that the highest ionic conductivity could be achieved at the sintering temperature of 1200 °C, 100 °C lower than that of LSTZ/LSTH. LSNZ was electrochemically stable at voltage above 1.2 V vs. Li/Li$^+$, showing similar stability with LSTZ/LSTH. However, ionic conductivity of LSNZ was only 2×10^{-5} S cm^{-1} at 30 °C. Kong et al. [62] reported that by adding excess lithium (20%) and sintering aid (1 wt% B_2O_3), ionic conductivity of LSNZ could be increased. However, the best sample showed only 1.98×10^{-5} S cm^{-1} at 30 °C. La doping at Sr sites could further increase ionic conductivity to 3.33×10^{-5} S cm^{-1} at 30 °C for $Li_{3/8}Sr_{7/16-3x/2}La_xZr_{1/4}Nb_{3/4}O_3$ (x = 0.05) [63]. However, the ionic conductivity is one magnitude lower than that of LSTZ/LSTH. Secondly, interfacial problems between LSTZ/LSTH/LSNZ and electrode materials have been less studied, which are important factors influencing performance of ASSBs [64].

2.4. LISICON-type electrolytes

LISICON is abbreviation of lithium super ionic conductor. Hong et al. [65] firstly reported a LISICON-type solid electrolyte $Li_{14}Zn(GeO_4)_4$, which showed ionic conductivity of 1.25×10^{-1} S cm^{-1} at 300 °C. Two factors for fast alkali-ion (Li-ion) conduction were proposed, including size of bottlenecks between neighboring alkali-ion (Li-ion) positions and bonding energy between mobile alkali-ion (Li-ion) and network anion (O^{2-}). In the case of $Li_{14}Zn(GeO_4)_4$, $[Li_{11}Zn(GeO_4)]^{3-}$ forms the network, and the other three Li-ions can diffuse freely between interstitial positions in the network. Bottlenecks between the

interstitial positions are large enough for Li-ions to transport, and each O^{2-} is bonded to four network cations (Li^+, Zn^{2+}, Ge^{4+}) and has weak bonding with mobile Li-ion. However, Li-ions in $Li_{14}Zn(GeO_4)_4$ can only diffuse in two dimensions because of parallelogram shape of the bottlenecks. Detailed study revealed ionic conductivity of 2×10^{-6} S cm^{-1} at 50 °C and 1.3×10^{-6} S cm^{-1} at 33 °C [66,67]. Crystal structure of this type of solid electrolyte is related to γ-Li_3PO_4 [68]. For pure γ-Li_3PO_4, since there is no Li-ion occupying interstitial positions, Li-ions can only diffuse by vacancy mechanism, causing low ionic conductivity. Li-ion vacancies form in $Li_{14}Zn(GeO_4)_4$, if all P^{5+} and partial Li^+ are replaced by Ge^{4+} and Zn^{2+} in the pure γ-Li_3PO_4, respectively. Three mobile Li-ions in $Li_{14}Zn(GeO_4)_4$ occupy 4c and 4a interstitial positions inside the framework, thus, Li-ions can diffuse through both vacancy and interstitial mechanisms, and ionic conductivity is hence improved [65]. However, ionic conductivity of $Li_{14}Zn(GeO_4)_4$ was still too low to be used and it should be further studied for ASSBs and other devices.

Kuwano et al. [69] prepared new LISICON-type of solid electrolytes $Li_{3+x}Ge_xV_{1-x}O_4$ ($0 < x < 1$), among which two compositions $Li_{3.5}Ge_{0.5}VO_4$ and $Li_{3.6}Ge_{0.6}V_{0.4}O_4$ revealed high bulk and total ionic conductivities of 4×10^{-5} S cm^{-1} and ~10^{-5} S cm^{-1} at 18 °C, respectively. $Li_{3+x}Ge_xV_{1-x}O_4$ is a solid solution between γ_{II}-Li_3VO_4 and Li_4GeO_4, which shows the same structure as γ_{II}-Li_3PO_4. For γ_{II}-Li_3VO_4 there is no interstitial Li-ions, while in $Li_{3+x}Ge_xV_{1-x}O_4$, partial V^{5+} is replaced by Ge^{4+} and Li^+, and extra Li-ions occupies interstitial positions leading to high ionic conductivities. Furthermore, $Li_{3+x}Ge_xV_{1-x}O_4$ showed good thermal stability and was stable in contact with CO_2 in the ambient atmosphere. Hu et al. [70] prepared solid solutions between Li_4SiO_4 and Li_3PO_4, $Li_{4-x}Si_{1-x}P_xO_4$ ($0 < x < 1$). The highest ionic conductivity of $Li_{3.5}Si_{0.5}P_{0.5}O_4$ and $Li_{3.4}Si_{0.4}P_{0.6}O_4$ was about 10^{-6} S cm^{-1} at room temperature. Li_4SiO_4 and Li_3PO_4 could form solid solutions over the whole composition range. However, because the two end members have different structures, there existed a structural change at $x = 0.5$ for the solid solutions. At $x = 0.5$ and 0.6, with Si^{4+} partially substituting P^{5+}, interstitial Li-ions are introduced to the Li_3PO_4 structure, leading to increased ionic conductivities compared to Li_3PO_4. Song et al. [71] partially doped O^{2-} with Cl^-, and obtained LISION-type solid electrolytes $Li_{10.42}Si_{1.5}P_{1.5}Cl_{0.08}O_{11.92}$ and $Li_{10.42}Ge_{1.5}P_{1.5}Cl_{0.08}O_{11.92}$ with ionic conductivities of 1.03×10^{-5} S cm^{-1} and 3.7×10^{-5} S cm^{-1} at 27 °C, respectively. At the same time, these two solid electrolytes were stable with lithium and up to 9 V vs. Li/Li^+. Ionic radius of Cl^- is larger than that of O^{2-}, thus, partial substitution of O^{2-} by Cl^- could increase lattice constants and size of bottlenecks for Li-ion diffusion. At the same time, because electronegativity of Cl^- is smaller than that of O^{2-}, bonding between Li^+ and Cl^- is weaker than that between Li^+ and O^{2-}. Due to these effects, the Cl^- doped electrolytes showed high ionic conductivities. Deng at al [72]. studied Li_4SiO_4, $Li_{3.75}Si_{0.75}P_{0.25}O_4$, $Li_{4.25}Si_{0.75}Al_{0.25}O_4$, $Li_4Al_{0.33}Si_{0.33}P_{0.33}O_4$ and $Li_4Al_{1/3}Si_{1/6}Ge_{1/6}P_{1/3}O_4$ by experiments and simulations. Three Li-ion diffusion mechanisms were discovered from low to high temperatures: local oscillation, isolated hopping and superionic motion. Substitution of Si in Li_4SiO_4 by P, Al or Ge could induce mixed polyanion effect, which could lower temperature of transition between diffusion mechanisms and increase ionic conductivity. By MD simulation, $Li_4Al_{1/3}Si_{1/6}Ge_{1/6}P_{1/3}O_4$ was predicted to have ionic conductivity of 9×10^{-4} S cm^{-1} at room temperature, which is much higher than Li_4SiO_4.

Overall, ionic conductivity of LISICON-type solid electrolytes was too low to be used in ASSBs. Kamaya et al. [73] replaced O^{2-} in LISICON-type solid electrolytes with S^{2-}, and obtained thio-LISICON-type $Li_{10}GeP_2S_{12}$ with ionic conductivity of 1.2×10^{-2} S cm^{-1} at room temperature, which was comparable to organic liquid electrolytes. The sulfide-type solid electrolytes will be introduced in section 2.7.

2.5. LiPON-type electrolytes

LiPON is abbreviation of lithium phosphorus oxynitride. Different from other electrolytes discussed above, LiPON is a kind of amorphous Li-ion solid electrolyte. Bates et al. [74] firstly synthesized LiPON using radio frequency (RF) magnetron sputtering with Li_3PO_4 as target in a pure N_2 atmosphere. Ionic conductivity of this solid electrolyte was about 2×10^{-6} S cm^{-1} at 25 °C, and stable with lithium. Suzuki et al. [75] modified composition of target to a mixture of Li_3PO_4 and Li_2O with molar ratio of 1:2, and ionic conductivity of prepared LiPON was improved to 6.4×10^{-6} S cm^{-1} at 25 °C, which was three times of that of conventional LiPON prepared from pure Li_3PO_4. The enhancement of ionic conductivity was due to increase of Li-ions inside the electrolyte. However, further increase in Li-ion amount in the target mixture led to decrease of ionic conductivity, which was probably caused by decrease of relative amount of phosphate chains which could promote Li-ion conduction. Li et al. [76] prepared LiPON films by ion beam assisted deposition (IBAD), which could control nitrogen content by adjusting flow ratio of N_2 and Ar. When the flow ratio was 1:8, the nitrogen doping reached the maximum, and the film showed the best mechanical properties and the highest ionic conductivity of 4.5×10^{-6} S cm^{-1} at room temperature. Su et al. [77] prepared LiPON films with high nitrogen content by RF magnetron sputtering, which showed mean ionic conductivity of 4.9×10^{-6} S cm^{-1} at 22 °C and transparency of higher than 80% in visible light range. Fujibayashi et al. [78] reported LiPON films prepared by metalorganic-chemical vapor deposition (MOCVD), which showed high ionic conductivities of 5.9×10^{-6} S cm^{-1} and 5.3×10^{-6} S cm^{-1} for thickness of 190 nm and 95 nm, respectively. Van-Jodin et al. [79] deposited LiPON films by RF sputtering in two ways: without magnetron (non-standard) and with magnetron (standard). The non-standard LiPON showed ionic conductivity of 6.7×10^{-6} S cm^{-1} at 24 °C, which was much higher than that of the standard LiPON (1.4×10^{-6} S cm^{-1} at 24 °C). In the standard LiPON, only one type of phosphate group PO_4^{3-} was observed, while in the non-standard LiPON, there also existed some other phosphate groups including PO_3^{2-} and PO_2^-. These phosphate groups could cause disorder in the structure, which led to higher Li-ion mobility in the non-standard LiPON. Several deposition parameters were studied for their effects on LiPON electrolytes, including RF power, N_2 pressure, target-substrate distance and target density [80]. The deposition rate would be higher with higher RF power, lower N_2 pressure, smaller target-substrate distance and higher target density. The prepared LiPON films showed ionic conductivities between 2.5×10^{-7} S cm^{-1} and 1.8×10^{-6} S cm^{-1} at 25 °C, and lower RF power, higher N_2 pressure, smaller target-substrate distance and higher target density could lead to higher ionic conductivity. It was demonstrated that ionic conductivity increased with N/P ratio, which could be increased by lower RF power, higher N_2 pressure and smaller target-substrate distance. N incorporation into LiPON was affected by reaction between N_2 gas and thin film surface, poisoning effect of target etc. Because LiPON film was very thin and exhibited low resistance, it was used for thin-film ASSBs and excellent charge-discharge properties were achieved [81,82]. Structure of a LiPON based thin-film battery is shown in Fig. 4 [82]. In this thin-film battery, cathode, anode, electrolyte and current collectors were deposited from vapor phases, and protective coating on the top could prevent Li anode from reaction with air. At the same time, LiPON-type solid electrolytes were stable at voltage of 0–~5.5 V vs. Li/Li^+, enabling use of many types of electrode materials in thin-film ASSBs [83].

Though LiPON-type solid electrolytes are promising for thin-film ASSBs, they are not appropriate for bulk ASSBs because of low room temperature ionic conductivities of 10^{-6}-10^{-5} S cm^{-1} [74,75,80].

2.6. Li_3N-type electrolytes

Li_3N solid electrolyte was prepared by reaction of pure lithium ribbon with nitrogen followed by cold-pressing and sintering in

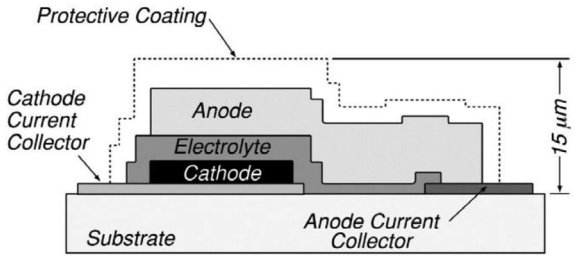

Fig. 4. Structure of a LiPON based thin-film ASSB. Reprinted from Ref. [82] with permission from Elsevier.

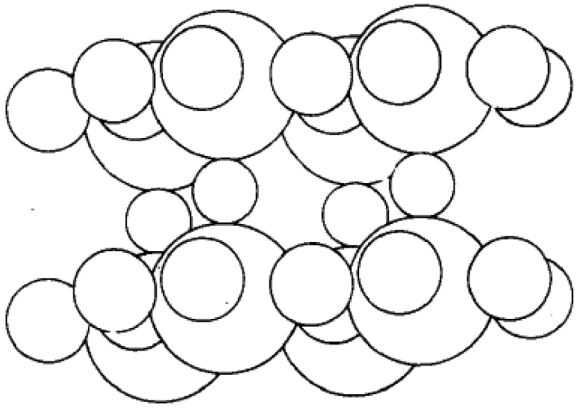

Fig. 5. Crystal structure of Li_3N, large and small circles represent nitrogen and lithium atoms. Reprinted from Ref. [10] with permission from Elsevier.

nitrogen at 650 °C [10]. The obtained Li_3N showed density of about 80% of theoretical density and exhibited ionic conductivity of 3.7×10^{-8} S cm^{-1} at 25 °C, which was lower than 3.0×10^{-7} S cm^{-1} of 96% pure Li_3N purchased from ROC/RIC company, but higher than that of a loose powder of Li_3N. The higher ionic conductivity of the 96% pure Li_3N was probably due to some dopants in the electrolyte. Li_3N annealed at about 750 °C in 1 atm of nitrogen attained high ionic conductivity of 2.0×10^{-4} S cm^{-1} at 25 °C [84]. It was assumed that the high temperature annealing increased Li/N ratio in the electrolyte, thus led to the high ionic conductivity. Rea et al. [85] prepared Li_3N electrolyte by reaction between lithium rod and nitrogen in a nitrogen atmosphere, and sintered at 800 °C. Ionic conductivities measured by AC and DC methods were 4×10^{-4} S cm^{-1} and 2×10^{-4} S cm^{-1} at 25 °C, respectively. Despite the high ionic conductivity, Li_3N could react with cathode materials with potential higher than 1.74 V vs. Li/Li$^+$ including TiS_2, PbI_2, PbS and AlI_3, indicating a narrow electrochemical stability window. Crystal structure of Li_3N is shown in Fig. 5 [10]. It is consisted of hexagonal Li_2N layers, which are connected by Li-ions to form N-Li-N bridges, and Li-ions can diffuse inside the 2-dimensional tunnels. Color of the Li_3N ranges between ruby red and violet black, suggesting covalent bonding between atoms.

Lithium nitride halides were demonstrated to be solid electrolytes with high Li-ion conductivities [86,87]. Kitahama et al. [88] studied solid electrolytes in Li_3N-LiCl system. The electrolytes in the composition range of $2Li_3N{\cdot}3LiCl$ to $9Li_3N{\cdot}11LiCl$ showed cubic antifluorite structures, and a new phase of $Li_9N_2Cl_3$ was found with non-cubic structure. The new $Li_9N_2Cl_3$ phase showed the highest ionic conductivity among the Li_3N-LiCl system, which was higher than 10^{-7} S cm^{-1} at room temperature. Hatake et al. [89] prepared $3Li_3N$-MI (M = Li, Na, K, Rb) solid electrolytes by solid-state reaction at 600 °C, and the electrolytes showed ionic conductivities of 7.0×10^{-5} S cm^{-1} to 1.1×10^{-4} S cm^{-1} at room temperature and decomposition voltages of 2.5–2.8 V. The total ionic conductivities were almost equal to bulk ionic conductivities, while grain boundary resistances were negligible because of good sinterability. At the same time, pressed compacts of the electrolyte powder exhibited ionic conductivities of higher than 10^{-5} S cm^{-1} at room temperature. Grain boundary resistances of the pressed compacts were higher than those of the sintered electrolytes, but the total ionic conductivities were not much lower than the bulk ionic conductivities, due probably to incorporation of iodide ions in the electrolytes. Due to the relatively high ionic conductivities of the pressed compacts, ASSBs could be constructed by simply pressing. Li/$3Li_3N$-MI/TiS_2 batteries could support a constant load of 1 MΩ with current of 2.5 μA cm^{-2} at voltage above 2.2 V for more than 10 h. C/$3Li_3N$-KI/$LiTiS_2$ batteries could charge-discharge for 10 cycles with coulombic efficiency of higher than 87%.

Partial substitution of Li-ions in Li_3N by other cations were investigated. Li_3AlN_2 crystallized in cubic antifluorite structure showed ionic conductivity of 5×10^{-8} S cm^{-1} at room temperature and decomposition voltage of 0.85 V at 104 °C [90]. $LiSi_2N_3$ solid electrolytes were prepared by hot-pressing [91]. Addition of Y_2O_3, CaF_2 or B_2O_3 could densify the $LiSi_2N_3$ electrolyte. At sintering temperature of 1600 °C, B_2O_3-doped $LiSi_2N_3$ showed higher ionic conductivity (7.0×10^{-4} S cm^{-1} at 327 °C) than undoped $LiSi_2N_3$. The undoped $LiSi_2N_3$ showed the highest ionic conductivity of 1.2×10^{-3} S cm^{-1} at 327 °C. Ca doping in $LiSi_2N_3$ could enhance ionic conductivity [92]. Densified $Li_{0.85}Ca_{0.075}Si_2N_3$ showed ionic conductivity of 1.6×10^{-7} S cm^{-1} at 25 °C.

Li_3N-type solid electrolytes showed barely satisfactory ionic conductivities. However, the decomposition voltages were too low for high energy density ASSBs.

2.7. Sulfide-type electrolytes

Sulfide-type solid electrolytes are closely related to a LISICON-type solid electrolyte γ-Li_3PO_4, with S^{2-} replacing O^{2-} [93,94]. Interaction between S^{2-} and Li^+ is weaker than that between O^{2-} and Li^+. Thus, the sulfide-type solid electrolytes showed higher Li-ion mobility and ionic conductivities than the oxide-type counterparts [93]. Sulfide-type solid electrolytes can be classified into three types: glasses, glass-ceramics and ceramics, which all show ionic conductivities comparable to organic liquid electrolytes. Glass/glass-ceramic Li_2S-P_2S_5 and ceramic thio-LISICON $Li_{4-x}Ge_{1-x}P_xS_4$ ($0 < x < 1$) are the most promising ones.

Ceramic thio-LISICON $Li_{4-x}Ge_{1-x}P_xS_4$ ($0 < x < 1$) solid electrolytes have attracted great attention in recent years because of their superior properties [73,94]. Based on LISICON-type solid electrolytes, Kanno et al. [95] replaced O^{2-} with S^{2-}, and prepared six new thio-LISICON electrolytes: Li_2GeS_3, Li_4GeS_4, Li_2ZnGeS_4, $Li_{4-2x}Zn_xGeS_4$, Li_5GaS_4 and $Li_{4+x+\delta}(Ge_{1-\delta'-x}Ga_x)S_4$. Li_2ZnGeS_4, $Li_{4-2x}Zn_xGeS_4$ ($0.0 \le x \le 0.20$) and $Li_{4+x+\delta}(Ge_{1-\delta'-x}Ga_x)S_4$ were prepared based on Li_4GeS_4 with substitution of Li^+ by Zn^{2+} and substitution of Ge^{4+} by Ga^{3+}. $Li_{4+x+\delta}(Ge_{1-\delta'-x}Ga_x)S_4$ showed the highest ionic conductivity of 6.5×10^{-5} S cm^{-1} at 25 °C with x = 0.25. Furthermore, $Li_{4+x+\delta}(Ge_{1-\delta'-x}Ga_x)S_4$ was electrochemically stable up to 5 V vs. Li/Li$^+$. Based on Li_4GeS_4, new thio-LISICON solid electrolytes $Li_{4-x}Ge_{1-x}P_xS_4$ were prepared by partially doping P^{5+} at Ge^{4+} sites [94]. Ionic conductivity increased with P content and reached the maximum of 2.17×10^{-3} S cm^{-1} at 25 °C for x = 0.75. $Li_{3.25}Ge_{0.25}P_{0.75}S_4$ was electrochemically stable with lithium and up to 5 V vs. Li/Li$^+$. The $Li_{4-x}Ge_{1-x}P_xS_4$ ($0 < x < 1$) system can be divided into three composition regions with different superlattice structures: region I ($0 < x < 0.6$), region II ($0.6 < x < 0.8$) and region III ($0.8 < x < 1$). Based on Li_4GeS_4 parent lattice a × b × c, diffraction data of electrolytes in these three regions could be indexed to lattices of a × 3b × 2c, a × 3b × 3c and a × 3b × 2c, respectively. The different structures were probably caused by variation of cation ordering. For thio-LISICON based on Li_4SiS_4 and Li_4GeS_4, there exist two doping strategies to improve ionic conductivity: vacancy-doping ($Li_{4-x}Si_{1-x}P_xS_4$, $Li_{4-2x}Zn_xGeS_4$, $Li_{4-x}Ge_{1-x}P_xS_4$) and interstitial-doping ($Li_{4+x}Si_{1-x}Al_xS_4$, $Li_{4+x}Ge_{1-x}Ga_xS_4$), which creates Li-ion vacancies or Li-ion interstitials in the structures. The vacancy-doped germanium system $Li_{4-x}Ge_{1-x}P_xS_4$ showed the highest ionic conductivity. In 2011,

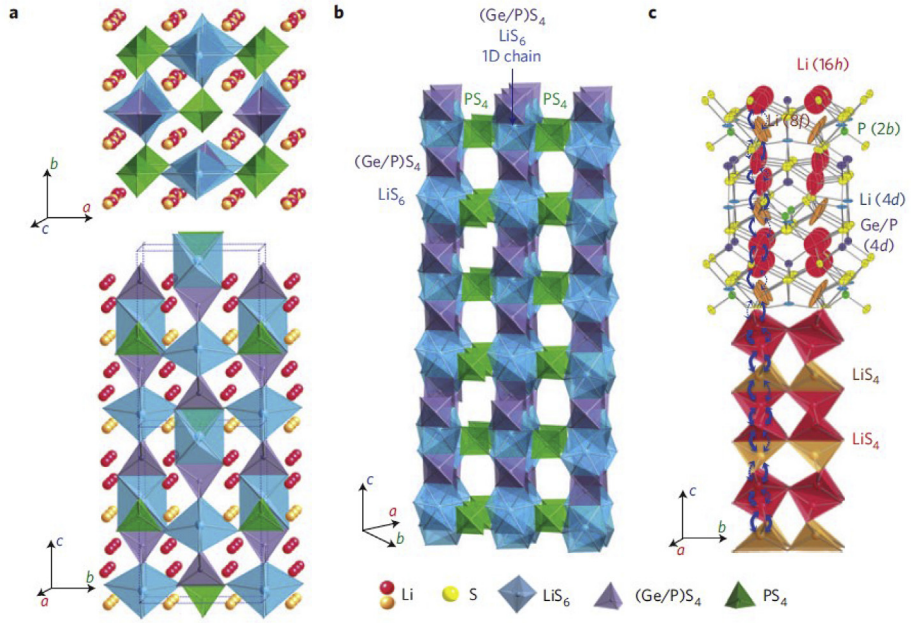

Fig. 6. Crystal structure of $Li_{10}GeP_2S_{12}$, (a) framework structure and mobile Li-ions, (b) framework structure showing 1-dimensional chains, (c) conduction pathways of Li-ions. Reprinted by permission from Macmillan Publishers Ltd: Nature Materials Ref. [73], copyright (2011).

Kamaya et al. [73] synthesized a new thio-LISICON solid electrolyte $Li_{10}GeP_2S_{12}$, showing high ionic conductivity of 1.2×10^{-2} S cm^{-1} at 27 °C. Though composition of $Li_{10}GeP_2S_{12}$ could be fitted to $Li_{4-x}Ge_{1-x}P_xS_4$ when x = 2/3 (thio-LISCION region II), this new solid electrolyte showed different structure with previously synthesized thio-LISICON $Li_{4-x}Ge_{1-x}P_xS_4$ ($0 < x < 1$). Crystal structure of $Li_{10}GeP_2S_{12}$ is shown in Fig. 6 [73]. Its 3-dimensional framework is composed of $(Ge_{0.5}P_{0.5})S_4$ tetrahedrons, PS_4 tetrahedrons, LiS_4 tetrahedrons and LiS_6 octahedrons. The $(Ge_{0.5}P_{0.5})S_4$ tetrahedrons and the LiS_6 octahedrons connect each other to form 1-dimensional chains along c-axis, and these chains are connected by the PS_4 tetrahedrons. Li-ions inside the LiS_4 tetrahedrons (16 h and 8f sites) form the 1-dimensional conduction pathways. It was found by neutron diffraction that thermal vibration of Li-ions at the 16 h and 8f sites were highly anisotropic, and the Li-ions were displaced toward interstitial positions between two 16 h sites and between 16 h and 8f sites, which demonstrated existence of the 1-dimensional conduction pathways. The high ionic conductivity of $Li_{10}GeP_2S_{12}$ is superior to those of other solid electrolytes, and comparable to those of organic liquid electrolytes. Even at low temperatures, $Li_{10}GeP_2S_{12}$ still showed satisfactory ionic conductivity of 1×10^{-3} S cm^{-1} at − 30 °C and 4×10^{-4} S cm^{-1} at − 45 °C. At the same time, $Li_{10}GeP_2S_{12}$ was stable with lithium and up to 5 V vs. Li/Li$^+$. A $LiCoO_2$/$Li_{10}GeP_2S_{12}$/In battery was successfully demonstrated to charge-discharge for 8 cycles with capacity over 120 mAh g^{-1}.

Mo et al. [96] studied $Li_{10}GeP_2S_{12}$ (LGPS) by first principles calculation, and it was predicted that LGPS was a 3-dimensional Li-ion conductor, and Li-ion diffusion in ab plane was not as fast as in c direction. Li-ions in LiS_6 octahedrons could participate in conduction in ab plane. Ionic conductivities in c direction and in ab plane were predicted to be 4×10^{-2} S cm^{-1} and 9×10^{-4} S cm^{-1} at 27 °C, respectively. However, diffusion in ab plane is important for the overall diffusion, because Li-ions can crossover between 1-dimensional channels in c direction. At the same time, it showed that LGPS was not stable against lithium, and decomposition voltage of LGPS was lower than 5 V, which was inconsistent with reported experimental results. It was proposed that decomposition of LGPS could form Li_2S or P_2S_5 in interfaces between electrolyte and electrodes, which became passivation layers to prevent LGPS from further decomposition. Ong et al. [97] studied $Li_{10\pm1}MP_2X_{12}$ (M = Ge, Si, Sn, Al, P; X = O, S, Se) family by first principles calculation. Cation-substituted $Li_{10}SiP_2S_{12}$, $Li_{10}SnP_2S_{12}$, $Li_{11}AlP_2S_{12}$ and $Li_9P_3S_{12}$ showed similar properties with $Li_{10}GeP_2S_{12}$. Oxygen-substituted $Li_{10}MP_2O_{12}$ (M = Ge, Si, Sn, Al, P) showed lower ionic conductivities and were less stable. The lower ionic conductivity of $Li_{10}GeP_2O_{12}$ than that of $Li_{10}GeP_2S_{12}$ was probably due to smaller anion radius and polarizability of O^{2-}, as observed in comparison between LISICON and thio-LISICON. Selenium-substituted $Li_{10}MP_2Se_{12}$ (M = Ge, Si, Sn, Al, P) showed larger cell volumes, but only marginally higher ionic conductivities than the sulfide counterparts. Study on effect of lattice parameter of $Li_{10}GeP_2S_{12}$ showed that decrease of lattice parameter could decrease ionic conductivity significantly, while increase of lattice parameter could only increase ionic conductivity by small amount. Thus, it can be concluded that in the thio-LISICON structure, S^{2-} is near optimal for Li-ion conduction. Considering low availability of selenium, air and moisture sensitivity of $Li_{10}GeP_2S_{12}$ cannot be addressed by substitution of S by other anions.

Sun et al. [98] substituted partial sulfur in $Li_{10}GeP_2S_{12}$ by oxygen to prepare $Li_{10}GeP_2S_{12-x}O_x$ ($0 \le x < 0.9$) electrolytes. $Li_{10}GeP_2S_{11.7}O_{0.3}$ and $Li_{10}GeP_2S_{11.4}O_{0.6}$ showed ionic conductivities of 1.03×10^{-2} S cm^{-1} and 8.43×10^{-3} S cm^{-1} at 25 °C, respectively, which are not much lower than that of $Li_{10}GeP_2S_{12}$ (1.2×10^{-2} S cm^{-1} at 27 °C). Incorporation of oxygen could promote electrochemical stability of the electrolyte. Kato et al. [99] reported that Cl-doped Si-analogue of $Li_{10}GeP_2S_{12}$, $Li_{9.54}Si_{1.74}P_{1.44}S_{11.7}Cl_{0.3}$ showed ionic conductivity of 2.5×10^{-2} S cm^{-1} at room temperature, which is the highest among the reported Li-ion electrolytes. Richards et al. [100] predicted highly conductive electrolyte $Li_{1+2x}Zn_{1-x}PS_4$ ($0 \le x \le 0.5$) by ab initio computation. Calculated ionic conductivity of $Li_2Zn_{0.5}PS_4$ was 5.38×10^{-2} S cm^{-1} at room temperature, showing promising potential.

Prior to development of ceramic thio-LISICON solid electrolytes, investigation focus of sulfide-type solid electrolytes was glass and glass-ceramic Li_2S-P_2S_5 [93,101]. Mizuno et al. [102] prepared ceramic, glass and glass-ceramic $70Li_2S$-$30P_2S_5$ solid electrolytes. The glass and glass-ceramic samples showed high ionic conductivities of 5.4×10^{-5} S cm^{-1} and 3.2×10^{-3} S cm^{-1} at room temperature, respectively. However, ionic conductivity of the ceramic sample prepared by solid-state reaction was only 2.6×10^{-8} S cm^{-1} at room temperature, and low conductive Li_3PS_4 and $Li_4P_2S_6$ phases were identified.

Thus, solid-state reaction method is not appropriate for Li_2S-P_2S_5 solid electrolytes to obtain high ionic conductivity. Zhang et al. [103] prepared $0.33[(1-y)B_2S_3$-$yP_2S_5]$-$0.67Li_2S$ ($0 \le y \le 0.3$, $0.9 \le y \le 1.0$) glasses by melt-quench. Because of existence of two network formers, the obtained glass solid electrolytes showed higher ionic conductivities than the single network former glasses $(1-x)B_2S_3$-xLi_2S ($0.5 \le x \le 0.75$) and $(1-x)P_2S_5$-xLi_2S ($0.5 \le x \le 0.7$). The glass $0.23B_2S_5$-$0.10P_2S_5$-$0.67Li_2S$ ($y = 0.3$) showed the highest ionic conductivity of 1.41×10^{-4} S cm^{-1} at 25 °C. Hayashi et al. [104] prepared xLi_2S-$(100-x)P_2S_5$ glass solid electrolytes by mechanical milling, which was much easier than melt-quench. The mechanical milling could be performed at room temperature, and the obtained electrolyte powder could be applied to ASSBs by simply pressing. The glass formation region could be extended to $x = 80$ by mechanical milling, while by melt-quench glass could only form for $x \le 70$. Ionic conductivity of the xLi_2S-$(100-x)P_2S_5$ glass increased with lithium amount, and reached the maximum of 2×10^{-4} S cm^{-1} at 25 °C for $x = 75$, larger than that of $70Li_2S$-$30P_2S_5$ prepared by melt-quench (1.6×10^{-4} S cm^{-1} at 25 °C).

It was believed that glasses could have higher ionic conductivities than crystals because of larger free volume of glasses due to random and open structures [105]. However, Hayashi et al. [106] prepared glass-ceramic $80Li_2S$-$20P_2S_5$ by mechanical milling and heating, and the obtained glass-ceramic showed ionic conductivity of 9×10^{-4} S cm^{-1} at room temperature, which was higher than 2×10^{-4} S cm^{-1} of the pristine glass. Li_7PS_6 crystal phase was identified in the glass-ceramic. However, the Li_7PS_6 crystal prepared by solid-state reaction showed ionic conductivity of 8×10^{-5} S cm^{-1} at room temperature, which was about one magnitude lower than that of the glass-ceramic. It was presumed that the Li_7PS_6 crystallized from the glass was a high-temperature phase, which is different with thermodynamically stable Li_7PS_6 phase. This high temperature phase could have a similar structure with the glass solid electrolyte and exhibited high ionic conductivity. Another possible reason for the high ionic conductivity of the glass-ceramic was due to enhanced contact between glassy powders, which was caused by softening of the glassy powders during heating. Based on this finding, Tatsumisago et al. [93] have carried out intensive researches on Li_2S-P_2S_5 glass-ceramic solid electrolytes. Further study of $80Li_2S$-$20P_2S_5$ glass-ceramic showed that Li_3PS_4 and unknown crystals also precipitated from the glass, together with Li_7PS_6 [107]. Because Li_7PS_6 and Li_3PS_4 crystals prepared by solid-state reaction exhibited low ionic conductivities at room temperature, the high ionic conductivity of $80Li_2S$-$20P_2S_5$ glass-ceramic should be due to the stabilized high-temperature phases of Li_7PS_6 and Li_3PS_4 [106–108]. It was reported that Li_3PS_4 and Li_7PS_6 had phase transformation at 150–200 °C, which was an evidence for the existence of the high-temperature phases [108]. Ionic conductivity of glass-ceramic was dependent on precipitated crystalline phases, which were affected by heating temperature, lithium content etc [109]. For mechanically milled $75Li_2S$-$25P_2S_5$ and $80Li_2S$-$20P_2S_5$ glasses, multi-crystallization was found during heating. For $80Li_2S$-$20P_2S_5$ glass, thio-LISICON II, thio-LISICON III, Li_3PS_4 and Li_7PS_6 crystallized successively with increase of heating temperature. For $75Li_2S$-$25P_2S_5$ glass, the crystallization sequence was thio-LISICON III, Li_3PS_4 and $Li_4P_2S_6$. The thio-LISICON II and thio-LISICON III phases should be metastable, and the former one should have higher ionic conductivity. Thus, after heating-cooling run during conductivity measurement, $80Li_2S$-$20P_2S_5$ glass-ceramic showed ionic conductivity of 7.2×10^{-4} S cm^{-1} at room temperature, while that of $75Li_2S$-$25P_2S_5$ glass-ceramic was only 2.8×10^{-4} S cm^{-1}. Glass-ceramic $70Li_2S$-$30P_2S_5$ was obtained by mechanical milling and crystallization, and its ionic conductivity was 3.2×10^{-3} S cm^{-1} at room temperature [102]. For $70Li_2S$-$30P_2S_5$ glass-ceramic, highly conductive phase was precipitated from glass, which was identified to contain $P_2S_7^{4-}$. Ionic conductivity of the glass-ceramic was even higher than those of highly conductive thio-LISICONs, which mainly contained PS_4^{3-}. It was found that superionic metastable phases, including the thio-LISICON II analogue in $80Li_2S$-$20P_2S_5$ and the new crystal phase in $70Li_2S$-$30P_2S_5$, were important to obtain Li_2S-P_2S_5 glass-ceramics with high ionic conductivities [110]. Pyro-thiophosphate $P_2S_7^{4-}$ and ortho-thiophosphate PS_4^{3-} were suitable structural units for fast Li-ion conduction in Li_2S-P_2S_5 glass-ceramics. The metastable phases could not be prepared by solid-state reaction, and could only be precipitated from the glasses. Temperature of the heat treatment of the glasses should be controlled to be just above first crystallization temperatures to obtain and maintain the metastable phases, because too high temperature would lead to thermodynamically stable phases ($Li_4P_2S_6$ for $70Li_2S$-$30P_2S_5$, $Li_{3.55}P_{0.89}S_4$ for $80Li_2S$-$20P_2S_5$) which are less conductive. The new high-conductive crystalline phase was determined to be $Li_7P_3S_{11}$ by synchrotron X-ray powder diffraction, and this phase contained $P_2S_7^{4-}$ and PS_4^{3-} [111]. Li-ions are located around P_2S_7 ditetrahedrons and PS_4 tetrahedrons, and the fast Li-ion diffusion should be related to interstitial sites and open space between P_2S_7 ditetrahedrons and PS_4 tetrahedrons. $Li_7P_3S_{11}$ glass-ceramic was also prepared by melt-quench and heating [112]. The glass melt-quenched at 750 °C showed existence of PS_4^{3-} and $P_2S_7^{4-}$ groups, which was similar with the glass prepared by mechanical milling. However, $P_2S_6^{4-}$ was also found for the glasses melt-quenched at 820 °C and 900 °C, which could lead to $Li_4P_2S_6$ with low ionic conductivity of 10^{-8} S cm^{-1} at room temperature. The $70Li_2S$-$30P_2S_5$ ($Li_7P_3S_{11}$) glass and glass-ceramic melt-quenched at 750 °C showed ionic conductivities of 9.2×10^{-5} S cm^{-1} and 2.1×10^{-3} S cm^{-1} at room temperature, respectively, which were similar with those prepared by mechanical milling. Seino et al. [113] optimized heat treatment condition to obtain Li_2S-P_2S_5 glass-ceramic with $Li_7P_3S_{11}$ metastable phase. Unified glass-ceramic showed almost no grain boundaries in microstructure, while cold-pressed glass-ceramic still showed obvious grain boundaries. Due to the improved contact between grains, the unified glass-ceramic showed extremely high ionic conductivity of 1.7×10^{-2} S cm^{-1} at 25 °C, which is one magnitude higher than that of the cold-pressed glass-ceramic (1.4×10^{-3} S cm^{-1} at 25 °C). This high ionic conductivity is even higher than those of organic liquid electrolytes ($\sim 10^{-2}$ S cm^{-1} at room temperature), considering that Li-ion transport number of the glass-ceramic was almost unity. It is also noted that the glass-ceramic still showed the high ionic conductivity of about 10^{-3} S cm^{-1} at − 35 °C, demonstrating potential to be applied in low temperature circumstances. Chu et al. [114] investigated $Li_7P_3S_{11}$ glass-ceramic by computational and experimental methods. $Li_7P_3S_{11}$ prepared by spark-plasma sintering (SPS) showed ionic conductivity of 1.16×10^{-2} S cm^{-1} at 27 °C, which is much higher than that of cold-pressed electrolyte (1.3×10^{-3} S cm^{-1} at 27 °C). Ab initio molecular dynamics (AIMD) simulation revealed even higher bulk ionic conductivity of 5.7×10^{-2} S cm^{-1} at 27 °C. It was predicted that densification of the electrolyte could further increase the overall ionic conductivity.

Sulfide-type solid electrolytes showed high ionic conductivities comparable to organic liquid electrolytes. However, they were not stable in the ambient atmosphere because of reaction with moisture. Several Li_2S-P_2S_5 electrolytes have been studied on structural changes and generation of H_2S upon exposure to air [115]. $67Li_2S$-$33P_2S_5$ glass and Li_2S generated large amounts of H_2S, with large structural changes. For $67Li_2S$-$33P_2S_5$ glass, original $P_2S_7^{4-}$ group decomposed to OH and SH groups, and SH further reacted to form OH group and H_2S. For Li_2S crystal, LiOH and H_2S were formed. $75Li_2S$-$25P_2S_5$ glass and glass-ceramic showed almost no structural change and little H_2S generation, which was because original PS_4^{3-} group has good chemical stability against hydrolysis. Thus, in order to apply sulfide-type solid electrolytes in ASSBs, it is necessary to choose appropriate chemical composition and separate the batteries from the ambient atmosphere.

2.8. Argyrodite-type electrolytes

Argyrodite-type Li-ion solid electrolytes Li_6PS_5X (X = Cl, Br, I) were firstly synthesized by Deiseroth et al. [116], showing similar structures

as Cu^+ and Ag^+ argyrodites. The six sulfur and halogen atoms form 136 tetrahedral holes. Four of these holes are formed by sulfur atoms (S1) only, and are occupied by P atoms. The rest 132 holes are formed by sulfur atoms (S2) and halogen atoms (X), and are partially occupied by Li atoms. For Li_6PS_5I, sulfur and iodide atoms at S2 and X sites are fully ordered, while it is fully disordered for Li_6PS_5Cl. Li_6PS_5Br is consisted of both ordered and disordered structures, with 84% S and 16% Br at S2 sites and 60% Br and 40% S at X sites. Li_6PS_5Br showed the highest Li-ion mobility amongst Li_6PS_5X (X = Cl, Br, I), as indicated by nuclear magnetic resonance (NMR). Further experiments were conducted to measure ionic conductivities of these solid electrolytes [117,118]. Li_6PS_5I showed room temperature ionic conductivity of 3.6×10^{-7} S cm^{-1} [117], while that of Li_6PS_5Br was in range of 10^{-3}-10^{-2} S cm^{-1} [118]. Boulineau et al. [119] used high energy ball-milling and post-annealing to prepare Li_6PS_5X (X = Cl, Br, I). In the ball-milled samples, Li_6PS_5Cl, Li_6PS_5Br and Li_6PS_5I formed with crystallite size of ~15 nm, and ionic conductivities were 4.6×10^{-4} S cm^{-1}, 6.2×10^{-4} S cm^{-1} and 1.9×10^{-4} S cm^{-1} at 25 °C, respectively. After annealing, the electrolytes were almost pure with the argyrodite phases as major phases, and crystallite size increased to ~90 nm. The annealed Li_6PS_5Cl and Li_6PS_5Br showed similar ionic conductivities as the ball-milled samples, while that of Li_6PS_5I decreased to ~10^{-7} S cm^{-1} at 25 °C. With optimization of ball-milling time to 10 h, ionic conductivity of Li_6PS_5Cl could reach 1.33×10^{-3} S cm^{-1} at 25 °C. Furthermore, Li_6PS_5X (X = Cl, Br, I) had an electrochemical stability window of 0–7 V vs. Li/Li^+. Adams et al. [120–126] carried out intensive research on argyrodite-type solid electrolytes. Li_6PS_5X (X = Cl, Br, I) were prepared by mechanical milling followed by annealing at 550 °C for 5 h [120]. After ball-milling, only Li_2S, P_2S_5 and LiX (X = Cl, Br, I) were observed, and after annealing argyrodite phases finally formed. The three ball-milled samples showed ionic conductivities of 3.3×10^{-5} S cm^{-1}, 3.2×10^{-5} S cm^{-1} and 2.2×10^{-4} S cm^{-1} at room temperature, respectively. Those of the annealed Li_6PS_5Cl and Li_6PS_5Br increased to 1.9×10^{-3} S cm^{-1} and 6.8×10^{-3} S cm^{-1} at room temperature, respectively, while that of Li_6PS_5I surprisingly decreased to 4.6×10^{-7} S cm^{-1} at room temperature. Bond valence analysis showed that Li_6PS_5Cl and Li_6PS_5Br exhibited Li-ion diffusion pathways with low activation energies for long range transport, which was the reason for the high ionic conductivities. The lower activation energies found in NMR studies should be due to local Li-ion transport, rather than long range transport. It was found that disorder in S^{2-}/Cl^- or S^{2-}/Br^- could promote Li-ion mobility, while I^- could not exchange with S^{2-} due to larger size and Li_6PS_5I showed lower ionic conductivity than Li_6PS_5Cl and Li_6PS_5Br [121]. Argyrodites Li_6PO_5X (X = Cl, Br) were also reported. However, O^{2-} positions in Li_6PO_5X (X = Cl, Br) were different with S^{2-} positions in Li_6PS_5X (X = Cl, Br), resulting in low ionic conductivities of ~10^{-9} S cm^{-1} at room temperature. Evolution of S^{2-}/Cl^- disorder and ionic conductivity of Li_6PS_5Cl were investigated based on in-situ neutron diffraction [122]. During heating of ball-milled glass-ceramic Li_6PS_5Cl, argyrodite phase of Li_7PS_6 formed between 80 °C and 150 °C. Upon further heating to higher temperature, Cl was incorporated into Li_7PS_6, forming $Li_{7-x}PS_{6-x}Cl_x$. Impedance measurements indicated that the argyrodite phase formed at 110–130 °C, and the Cl incorporation happened at 170–200 °C. Li_6PS_5Cl heat-treated at 150, 200 and 250 °C showed ionic conductivities of 1.1×10^{-4} S cm^{-1}, 3.6×10^{-4} S cm^{-1} and 1.1×10^{-3} S cm^{-1} measured at 40 °C, respectively, demonstrating that the crystalline phase and the Cl incorporation were important for Li-ion conduction in the glass-ceramic Li_6PS_5Cl. Yu et al. [127] investigated effect of mechanical milling time on structure and ionic conductivity of Li_6PS_5Cl. Li_6PS_5Cl argyrodite phase formed after milled at 550 rpm for 4 h, and the ones milled for 8–16 h showed the highest ionic conductivities of ~1.0×10^{-3} S cm^{-1} at room temperature. Further annealing at 550 °C for 5 h could increase crystallinity and contact between grains, leading to higher ionic conductivity of 1.1×10^{-3} S cm^{-1} at room temperature. Zhang et al. [128] demonstrated that solid-state sintering was superior to mechanical alloying to obtain high ionic conductivity for Li_6PS_5X (X = Cl, Br, I) argyrodites. Li_6PS_5Cl and Li_6PS_5Br sintered with excess Li_2S showed ionic conductivities of 1.8×10^{-3} S cm^{-1} and 1.3×10^{-3} S cm^{-1} at room temperature, respectively. Schneider et al. [129] synthesized halogen-free and Si-containing argyrodite electrolytes, which could avoid the issues caused by halogens in conventional argyrodites. Substitution of partial phosphorous by silicon could stabilize the cubic high-temperature (HT) phase, which is more conductive than the orthorhombic low-temperature (LT) phase. The electrolytes with compositions $Li_{2x}SiP_2S_{7+x}$ ($10 < x < 12$) showed high ionic conductivities of about 3×10^{-3} S cm^{-1}, which is competitive with halogen-containing argyrodites.

Li_6PS_5Br solid electrolyte has been used to construct several ASSBs, including Cu-Li_2S/Li_6PS_5Br/In, CuS/Li_6PS_5Br/In-Li, S/Li_6PS_5Br/In-Li and MoS_2/Li_6PS_5Br/In-Li [123–126]. The Cu-Li_2S/Li_6PS_5Br/In battery showed high initial charge and discharge capacities of 500 mAh g^{-1} and 445 mAh g^{-1} (0.1C, theoretical capacity 490 mAh g^{-1}), respectively [123]. However, its reversible capacity was limited by cathode volume change and dropped to ~70 mAh g^{-1} after 20 cycles. During the initial discharging, two plateaus at 1.4 V and 0.9 V were observed, which were assigned to two-step reduction of CuS as indicated in Eqs. (3) and (4):

$$2.05\ \text{V vs. Li/Li}^+\ \ \text{CuS} + x\ \text{Li} \rightarrow \text{Li}_x\text{CuS}\ (0 < x < 1) \quad (3)$$

$$1.68\ \text{V vs. Li/Li}^+\ \ \text{Li}_x\text{CuS} + (2\text{-}x)\ \text{Li} \rightarrow \text{Cu} + \text{Li}_2\text{S} \quad (4)$$

The first step was an intercalation reaction with small volume change, and the second step was a conversion reaction accompanied with large volume change. During cycling, capacity in the conversion step decayed fast, while that of the intercalation step could maintain at a high level. The CuS/Li_6PS_5Br/In-Li battery showed an initial discharge capacity of 650 mAh g^{-1} (0.02C, theoretical capacity 560 mAh g^{-1}), while its reversible capacity after 20 cycles was only 90 mAh g^{-1} [124]. During discharging, Li_6PS_5Br in the cathode mixture could accommodate reduced Cu^+ to form $Cu_yLi_{6-y}PS_5Br$ with low ionic conductivity, which could cause increase of internal resistance of the battery. Volume change of the cathode caused by conversion reaction detached active materials from ionic conductive Li_6PS_5Br and electronic conductive carbon black. These effects resulted in formation of cracks and fast capacity fading. The S/Li_6PS_5Br/In-Li battery showed an initial discharge capacity of 1355 mAh g^{-1} (0.1C, theoretical capacity 1672 mAh g^{-1}) and a reversible capacity of 1080 mAh g^{-1} after 50 cycles [125]. By a two-step ball-milling, composite cathode consisted of amorphous sulfur, super P carbon and crystalline Li_6PS_5Br was obtained with particle size of 100 nm, which showed high homogeneity and intimate contact between the components. Li_6PS_5Br was stable during the cycling, leading to better cycling stability of S/Li_6PS_5Br/In-Li than Cu-Li_2S/Li_6PS_5Br/In and CuS/Li_6PS_5Br/In-Li batteries. Furthermore, it was noted that sulfur content in cathode should be selected carefully, considering balance between capacity and volume change. The MoS_2/Li_6PS_5Br/In-Li battery was transformed into a Li/S battery after fully discharging [126]. Mo particles with 3 nm in size were dispersed in the cathode, enhancing electronic conductivity. The battery showed an initial discharge capacity of 650 mAh g^{-1} (0.1C, theoretical capacity 670 mAh g^{-1}) in 0.1–3 V, and a reversible capacity of 190 mAh g^{-1} in 1–3 V after 40 cycles with coulombic efficiency of close to 100%. At 70 °C, the battery showed a reversible capacity of 315 mAh g^{-1} (0.2C) between 0.6 and 3.1 V after 200 cycles, and capacity retention maintained at 85% after 700 cycles, which is even better than liquid electrolyte based MoS_2 battery operated at room temperature for 100 cycles.

Argyrodite-type solid electrolytes are very promising for ASSBs. However, similar with sulfide-type solid electrolytes, argyrodite-type solid electrolytes could not be exposed to air, which restricts its application to a large extent. Effective and convenient battery construction technologies are required to conquer the stability problems.

2.9. Anti-perovskite-type electrolytes

Anti-perovskite-type solid electrolytes were designed and fabricated based on changing perovskite system from $A^+B^{2+}X_3^-$ to $A^-B^{2-}X_3^+$, where A site atom is halogen (F, Cl, Br, I) or a mixture of halogens, B site atom is oxygen and X site atom is lithium [11]. Li_3OCl and Li_3OBr showed typical perovskite structures, and $Li_3O(Cl_{1-z}Br_z)$ could be formed by solid solutions between the two end members. Li_3OCl and $Li_3OCl_{0.5}Br_{0.5}$ showed ionic conductivities of 8.5×10^{-4} S cm^{-1} and 1.94×10^{-3} S cm^{-1} at room temperature, respectively. The higher ionic conductivity was obtained for $Li_3OCl_{0.5}Br_{0.5}$ because it could avoid small Li-ion hopping interstitial space in Li_3OBr and structural distortion in Li_3OCl. It was suggested that by adopting A-mixing, M-doping and LiA-depletion schemes, $Li_{3-x-\delta}M_{x/2}O(A_{1-z}A'_z)_{1-\delta}$ could be prepared with even higher ionic conductivities. Beyond this, easy fabrication, low-cost and environmental friendly starting materials etc. made the anti-perovskites promising solid electrolytes.

First principles calculation of Li_3OCl and Li_3OBr solid electrolytes showed a low-barrier hop mechanism with an interstitial dumbbell for Li-ion diffusion [130]. Diffusion through vacancy mechanism had energy barriers of 340 meV and 375 meV for Li_3OCl and Li_3OBr, respectively, while those of the interstitial dumbbell hop mechanism were much smaller as 170 meV and 175 meV, respectively. Thus, formation of Li-ion interstitial dumbbells contributed to superionic conductivities of the anti-perovskites. Zhang et al. [131] suggested that perfect anti-perovskite structure could not exhibit superionic conduction because of lack of Li-ion diffusion pathway, and some structural defects should be induced during experimental preparation. One vacancy was introduced into anti-perovskite structures, and simulation results showed much improved diffusion mobility of Li-ions. Furthermore, introduction of one Cl-O exchange disorder in Li_3OCl structure resulted in even higher Li-ion diffusion mobility. Ionic conductivities of Li_3OCl and $Li_3OCl_{0.5}Br_{0.5}$ with a Li-ion vacancy were extrapolated to be 1.2×10^{-4} S cm^{-1} and 2.1×10^{-4} S cm^{-1} at 27 °C, respectively, which were several times smaller than experimental values. Thus, more defects should be introduced in the structures to rationalize the diffusion mechanism. Deng et al. [132] studied $Li_3OCl_{1-x}Br_x$ by first principles calculation and percolation theory, and predicted that the electrolytes with $0.235 \leq x \leq 0.395$ showed high ionic conductivities. Through ab initio molecular dynamics (AIMD) simulation, $Li_3OCl_{0.75}Br_{0.25}$ was predicted to be more conductive than $Li_3OCl_{0.5}Br_{0.5}$.

Braga et al. [133] prepared glass electrolytes $Li_{3-2x}M_xHalO$ (M = Mg, Ca, Ba; Hal = Cl, or a mixture of halogens) from anti-perovskite crystals, and $Li_{3-2x}Ba_xClO$ (x = 0.005) showed ionic conductivity of 2.5×10^{-2} S cm^{-1} at 25 °C, which was the highest among solid electrolytes at that time. Based on compositions Li_3OA (A = halogen), Fang et al. [134] predicted new anti-perovskites $Li_3O(BH_4)$ and $Li_3O(BH_4)_{0.5}Cl_{0.5}$ by replacing halogens by BH_4 superhalogens. MD simulations estimated ionic conductivities of $Li_3O(BH_4)$ and $Li_3O(BH_4)_{0.5}Cl_{0.5}$ to be 1.0×10^{-4} S cm^{-1} and 2.1×10^{-4} S cm^{-1} at room temperature, respectively. It was predicted that experimental ionic conductivity of $Li_3O(BH_4)_{0.5}Cl_{0.5}$ could be higher than 10^{-3} S cm^{-1} at room temperature, considering underestimation caused by calculation. Li_3SBF_4 and $Li_3S(BF_4)_{0.5}Cl_{0.5}$ were also predicted and estimated to have ionic conductivities of 10^{-2} S cm^{-1} and 10^{-1} S cm^{-1} at room temperature, respectively [135]. Lü et al. [136] deposited a thin-film anti-perovskite Li_3OCl solid electrolyte by pulse laser deposition (PLD) from a composite target consisted of Li_2O and LiCl, achieving ionic conductivity of 2.0×10^{-4} S cm^{-1} at room temperature, which is higher than that of the Li_3OCl film prepared from Li_3OCl compound target (9×10^{-6} S cm^{-1}). It was indicated that the Li_3OCl film prepared from the composite target had larger grain size and higher crystallinity than the Li_3OCl film prepared from the compound target. Based on this solid electrolyte, a thin-film ASSB $LiCoO_2$/Li_3OCl/graphite was constructed through layer-by-layer deposition, as shown in Fig. 7 [136]. The battery showed an initial discharge capacity of 120 mAh g^{-1} (10 mA g^{-1}, theoretical capacity 274 mAh g^{-1}) in 2.2–4.2 V. However, the capacity dropped to about 66 mAh g^{-1} after 20 cycles, probably due to irreversible side reactions and unsatisfactory battery sealing. Coulombic efficiency after the first cycle was relatively low at ~95%, indicating ionic conductivity of the electrolyte was still not high enough for battery.

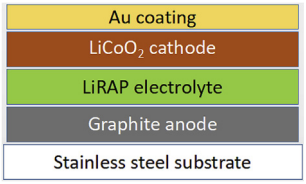

Fig. 7. A thin-film ASSB based on an anti-perovskite solid electrolyte [136].

Anti-perovskite-type solid electrolytes had high ionic conductivities, and are promising for bulk and thin-film ASSBs. However, they are very hygroscopic and should be operated in an inert atmosphere, posing difficulties for application in ASSBs [11].

3. Summary of properties of solid electrolytes

Several types of solid electrolytes are introduced, and each of them has respective advantages and drawbacks. Properties of these solid electrolytes are summarized in Table 1.

According to Table 1, advantages and drawbacks of these solid electrolytes are summarized as below:

a. NASICON-type of LAGP has high ionic conductivity and good chemical and electrochemical stability. However, one of the LAGP precursor, GeO_2, is expensive and can significantly increase cost of LAGP based ASSBs. It is necessary to develop cost effective new NASICON.
b. Garnet-type of Al-stabilized LLZO has high ionic conductivity and is stable with lithium. However, it is not stable in contact with moisture or CO_2 in the ambient atmosphere. It is important to improve LLZO stability through material modifications.
c. Perovskite-type of LSTZ/LSTH is promising for application in ASSBs. However, its preparation condition is very harsh and ionic conductivity is not high enough yet.
d. LISICON-type of solid electrolytes have good chemical and electrochemical stability, but low ionic conductivities compared with other oxide solid electrolytes.
e. LiPON-type of solid electrolytes have been applied and are suitable in thin-film ASSBs, but they are not proper for bulk ASSBs because of low ionic conductivities of 10^{-6}-10^{-5} S cm^{-1} at room temperature.
f. Although Li_3N-type of solid electrolytes have reasonable ionic conductivities, their decomposition voltages are too low for high energy density ASSBs.
g. Sulfide-type of solid electrolytes have the highest ionic conductivities in the magnitude of 10^{-2} S cm^{-1} at room temperature. However, they are not stable in the ambient atmosphere because of reaction with moisture. Hence they have to be used in a controlled atmosphere for bulk batteries but not for thin-film ones because of immature deposition technologies for sulfide electrolytes.
h. Argyrodite-type of solid electrolytes possess high ionic conductivities. Similar to sulfide-type solid electrolytes, they are not stable in the ambient atmosphere. Suitable encapsulation of cells using argyrodite-type solid electrolytes is essential, otherwise it may also cause safety issues.
i. Anti-perovskite-type of solid electrolytes have high ionic conductivities and can be applied in bulk and thin-film ASSBs. However, they are very hygroscopic and operation in an inert atmosphere is required.

Table 1
Summary of properties of solid electrolytes.

Electrolyte	Prototype	Composition	Ionic conductivity ($S\ cm^{-1}$)	Electrochemical stability vs. Li/Li^+
NASICON	$LiTi_2(PO_4)_3$	$LiTi_2(PO_4)_3$ [27]		> 2.5 V
		$LiTi_2(PO_4)_3$-0.2Li_3BO_3 [18]	3×10^{-4} (25 °C)	
		$Li_{1.3}Al_{0.3}Ti_{1.7}(PO_4)_3$ [17]	7×10^{-4} (25 °C)	reduced by Li
		$Li_{1.3}M_{0.3}Ti_{1.7}(PO_4)_3$ (M = Al, Sc) [20]	7×10^{-4} (25 °C)	
		2[$Li_{1.4}Ti_2Si_{0.4}P_{2.6}O_{12}$]-$AlPO_4$ [22]	1.5×10^{-3} (RT)	
		100[$Li_{1.5}Cr_{0.5}Ti_{1.5}(PO_4)_3$]-5$SiO_2$ [23]	2.14×10^{-2} (25 °C)	
	$LiGe_2(PO_4)_3$	$Li_{1.5}Al_{0.5}Ge_{1.5}(PO_4)_3$ [28]	4.0×10^{-4} (RT)	0.85–7 V [34]
		$Li_{1.5}Al_{0.5}Ge_{1.5}(PO_4)_3-0.05Li_2O$ [29]	7.25×10^{-4} (RT)	0.5–6 V
		19.75Li_2O· 6.17Al_2O_3· 37.04GeO_2· 37.04 P_2O_5 [30]	5.08×10^{-3} (27 °C)	
		$Li_{1.5}Al_{0.4}Cr_{0.1}Ge_{1.5}(PO_4)_3$ [31]	6.65×10^{-3} (26 °C)	0.44–7 V
Garnet	$Li_7La_3Zr_2O_{12}$	$Li_7La_3Zr_2O_{12}$ [40]	3×10^{-4} (25 °C)	
		$Li_{6.75}La_3(Zr_{1.75}Nb_{0.25})O_{12}$ [42]	8×10^{-4} (25 °C)	0-9 V
		$Li_{7.06}La_3Y_{0.06}Zr_{1.94}O_{12}$ [43]	8.10×10^{-4} (25 °C)	
		$Li_{6.4}La_3Zr_{1.4}Ta_{0.6}O_{12}$ [44]	1.0×10^{-3} (RT)	0-5 V
		$Li_{6.55}Ga_{0.15}La_3Zr_2O_{12}$ [45]	1.3×10^{-3} (24 °C)	
		$Li_{6.4}Ga_{0.2}La_3Zr_2O_{12}$ [46]	1.32×10^{-3} (20 °C)	
		$Li_{6.25}Ga_{0.25}La_3Zr_2O_{12}$ [47]	1.46×10^{-3} (25 °C)	
		$Li_{6.20}Ga_{0.30}La_{2.95}Rb_{0.05}Zr_2O_{12}$ [49]	1.62×10^{-3} (RT)	
		$Li_{6.65}Ga_{0.15}La_3Zr_{1.90}Sc_{0.10}O_{12}$ [48]	1.8×10^{-3} (27 °C)	
Perovskite	$Li_{3x}La_{2/3-x}TiO_3$	$Li_{0.34(1)}La_{0.51(1)}TiO_{2.94(2)}$ [52]	2×10^{-5} (RT)	
		$Li_{0.35}La_{0.55}TiO_3$ [55]		> 1.8 V
		$LiSr_{1.65}Zr_{1.3}Ta_{1.7}O_9$ [57]	1.3×10^{-5} (30 °C)	
		$Li_{3/8}Sr_{7/16}Ta_{3/4}Zr_{1/4}O_3$	8×10^{-5} (30 °C) [7]	> 1.0 V [7]
			2.7×10^{-4} (27 °C) [58]	
			2×10^{-4} (27 °C) [59]	
		$Li_{3/8}Sr_{7/16}Ta_{3/4}Hf_{1/4}O_3$ [60]	3.8×10^{-4} (25 °C)	1.4–4.5 V
		$Li_{3/8}Sr_{7/16}Nb_{3/4}Zr_{1/4}O_3$	2×10^{-5} (30 °C) [61]	> 1.2 V [61]
			1.98×10^{-5} (30 °C) [62]	
		$Li_{3/8}Sr_{0.3625}La_{0.05}Zr_{1/4}Nb_{3/4}O_3$ [63]	3.33×10^{-5} (30 °C)	
LISICON	γ-Li_3PO_4	$Li_{14}Zn(GeO_4)_4$ [67]	1.3×10^{-6} (33 °C)	
		$Li_{3+x}Ge_xV_{1-x}O_4$ (x = 0.5, 0.6) [69]	$\sim 10^{-5}$ (18 °C)	
		$Li_{4-x}Si_{1-x}P_xO_4$ (x = 0.5, 0.6) [70]	$\sim 10^{-6}$ (RT)	
		$Li_{10.42}Si_{1.5}P_{1.5}Cl_{0.08}O_{11.92}$ [71]	1.03×10^{-5} (27 °C)	0-9 V
		$Li_{10.42}Ge_{1.5}P_{1.5}Cl_{0.08}O_{11.92}$ [71]	3.7×10^{-5} (27 °C)	0-9 V
LiPON		Li_3PO_4 (target)	$\sim 2 \times 10^{-6}$ (25 °C) [74]	> 0 V [74]
			4.5×10^{-6} (RT) [76]	0- ~5.5 V [83]
			4.9×10^{-6} (22 °C) [77]	
			6.7×10^{-6} (24 °C) [79]	
			2.3×10^{-6} (25 °C) [83]	
		Li_3PO_4-2Li_2O (target) [75]	6.4×10^{-6} (25 °C)	
		LiO^tBu and TDMAP (precursors) [78]	5.9×10^{-6}	
Li_3N	Li_3N	Li_3N	3.0×10^{-7} (25 °C) [10]	< 1.74 V [85]
			2.0×10^{-4} (25 °C) [84]	
			4×10^{-4} (25 °C) [85]	
		$Li_6N_2Cl_3$ [88]	$> 10^{-7}$ (RT)	
		3Li_3N-MI (M = Li, Na, K, Rb) [89]	7.0×10^{-5}-1.1×10^{-4} (RT)	< 2.5–2.8 V
Sulfide	Li_4GeS_4	$Li_{4.25+8}(Ge_{0.75-8}Ga_{0.25})S_4$ [95]	6.5×10^{-5} (25 °C)	0-5 V
		$Li_{3.25}Ge_{0.25}P_{0.75}S_4$ [94]	2.17×10^{-3} (25 °C)	0-5 V
	$Li_{10}GeP_2S_{12}$	$Li_{10}GeP_2S_{12}$ [73]	1.2×10^{-2} (27 °C)	0-5 V
		$Li_{10}GeP_2S_{11.7}O_{0.3}$ [98]	1.03×10^{-2} (25 °C)	
		$Li_{9.54}Si_{1.74}P_{1.44}S_{11.7}Cl_{0.3}$ [99]	2.5×10^{-2} (RT)	
	Li_2S-P_2S_5	70Li_2S-30P_2S_5 glass	5.4×10^{-5} (RT) [102]	
			1.6×10^{-4} (25 °C) [104]	
			9.2×10^{-5} (RT) [112]	
		70Li_2S-30P_2S_5 glass-ceramic	3.2×10^{-3} (RT) [102]	
			2.1×10^{-3} (RT) [112]	
			1.7×10^{-2} (RT) [113]	
			1.16×10^{-2} (27 °C) [114]	
		0.23B_2S_5-0.10P_2S_5-0.67Li_2S glass [103]	1.41×10^{-4} (25 °C)	
		75Li_2S-25P_2S_5 glass [104]	2×10^{-4} (25 °C)	
		75Li_2S-25P_2S_5 glass-ceramic [109]	2.8×10^{-4} (RT)	
		80Li_2S-20P_2S_5 glass [106]	2×10^{-4} (RT)	
		80Li_2S-20P_2S_5 glass-ceramic	9×10^{-4} (RT) [106]	
			7.2×10^{-4} (RT) [109]	

(*continued on next page*)

Table 1 (*continued*)

Electrolyte	Prototype	Composition	Ionic conductivity (S cm^{-1})	Electrochemical stability vs. Li/Li^+
Argyrodite	Li_6PS_5X (X = Cl, Br, I)	Li_6PS_5Cl	1.33×10^{-3} (25 °C) [119] 1.9×10^{-3} (RT) [120] 1.1×10^{-3} (RT) [127] 1.8×10^{-3} (RT) [128]	0-7 V [119]
		Li_6PS_5Br	10^{-3}-10^{-2} (RT) [118] $\sim 6.2 \times 10^{-4}$ (25 °C) [119] 6.8×10^{-3} (RT) [120] 1.3×10^{-3} (RT) [128]	0-7 V [119]
		Li_6PS_5I	3.6×10^{-7} (RT) [117] $\sim 10^{-7}$ (25 °C) [119] 4.6×10^{-7} (RT) [120]	0-7 V [119]
		$Li_{2x}SiP_2S_{7+x}$ ($10 < x < 12$) [129]	$\sim 3 \times 10^{-3}$	
Anti-perovskite	Li_3OX (X = Cl, Br, I)	Li_3OCl	8.5×10^{-4} (RT) [11] 2.0×10^{-4} (RT) [136]	
		$Li_3OCl_{0.5}Br_{0.5}$ [11]	1.94×10^{-3} (RT)	
		$Li_{2.99}Ba_{0.005}ClO$ [133]	2.5×10^{-2} (25 °C)	

Generally speaking, NASICON-, garnet- and perovskite-type solid electrolytes are promising ones because of overall performance in ionic conductivity and chemical and electrochemical stability.

4. Application of solid electrolytes in all-solid-state lithium-ion batteries

Applications of the three promising types of oxide solid electrolytes (NASICON, garnet, perovskite) in ASSBs are tabulated in Table 2.

For NASICON-type electrolytes, ASSBs have been constructed by different methods such as sol-gel [137,138], screen-printing [139], deposition of electrode film on electrolyte [140] et al. Rho et al. [137] constructed an ASSB in the structure of $Li_4Ti_5O_{12}/LiTi_2(PO_4)_3$-$AlPO_4$/PMMA gel-polymer/Li. $Li_4Ti_5O_{12}$ was coated on surface of the solid electrolyte by sol-gel, spin coating and heating. Through the sol-gel method, interfacial contact area between $Li_4Ti_5O_{12}$ film and Li-$Ti_2(PO_4)_3$-$AlPO_4$ was increased, and the interfacial resistance was as low as $\sim 110\,\Omega\,cm^{-2}$. The ASSB could charge-discharge reversibly for 30 cycles, however, the initial discharge capacity was only 57% of the theoretical one, which was probably due to reaction between $Li_4Ti_5O_{12}$ and $LiTi_2(PO_4)_3$-$AlPO_4$ during heating. Dokko et al. [138] fabricated a $LiMn_2O_4$/LATP/PMMA gel-polymer/Li ASSB. $LiMn_2O_4$ was coated onto LATP by sol-gel, spin-coating and heating. The $LiMn_2O_4$ film showed high porosity with submicron-sized pores. The initial discharge capacity was only 54% of the theoretical one, which could be caused by isolation of some active materials due to porous nature and impurities inside $LiMn_2O_4$ or at the interface. Kobayashi et al. [139] fabricated a symmetric ASSB $Li_3V_2(PO_4)_3/Li_{1.5}Al_{0.5}Ge_{1,5}(PO_4)_3/Li_3V_2(PO_4)_3$. $Li_3V_2(PO_4)_3$ was coated onto both sides of $Li_{1.5}Al_{0.5}Ge_{1,5}(PO_4)_3$ by screen-printing and hot-pressing. The initial discharge capacity was only 58% of the theoretical one, which was due to large internal resistance. However, the symmetric cell configuration with all NASICON-type phosphate electrodes and electrolyte could benefit fabrication process of ASSBs. Kim et al. [140] constructed a $LiCoO_2$/LATP/LiPON/Li cell. $LiCoO_2$ was deposited onto LATP by magnetron sputtering and heating. The Coulombic efficiency of the first cycle was only 68%, leading to a low initial discharge capacity (57% of theoretical capacity). The large capacity loss was probably caused by structural defects in $LiCoO_2$ film. During cycling, there was continuous capacity fading, which could be caused by anode degradation. Anyway, the $LiCoO_2$/

Table 2
Summary of all-solid-state batteries.

Electrolyte	Cathode (mAh g^{-1})	Anode	Initial discharge capacity (mAh g^{-1})	Retention (mAh g^{-1})
$LiTi_2(PO_4)_3$-$AlPO_4$ [137]	$Li_4Ti_5O_{12}$ (175)	Li	100.49 (57%, 0.2 C)	~100 (30th)
$Li_{1+x}Al_xTi_{2-x}(PO_4)_3$ [138]	$LiMn_2O_4$ (148)	Li	80 (54%, 0.1 C)	
$Li_{1.5}Al_{0.5}Ge_{1.5}(PO_4)_3$ [139]	$Li_3V_2(PO_4)_3$ (66)	$Li_3V_2(PO_4)_3$	38 (58%, 0.1 C)	
Commercial LATP [140]	$LiCoO_2$ (140)	Li	80 (57%, 0.01 C)	~30 (50th)
$Li_7La_3Zr_2O_{12}$ [141]	$LiCoO_2$ (140)	Li	0.015 mAh cm^{-2} (0.2%, 0.00024 C)	~0.012 mAh cm^{-2} (3rd)
Nb-doped $Li_7La_3Zr_2O_{12}$ [142]	$LiCoO_2$ (115)	Li	85 (74%, 0.05 C)	~85 (5th)
$Li_7La_{2.75}Ca_{0.25}Zr_{1.75}Nb_{0.25}O_{12}$ [143]	$Li_2FeMn_3O_8$ (148)	Li	103 (70%, 0.1 C)	110 (50th)
$Li_{6.20}Ga_{0.30}La_{2.95}Rb_{0.05}Zr_2O_{12}$ (60 °C) [49]	$LiFePO_4$ (170)	Li	152 (88%, 0.05 C)	110 (20th)
$Li_7La_3Zr_2O_{12}$ [144]	$LiFePO_4$ (170)	Li	138 (81%, 1 C)	140 (100th)
$Li_{0.55}La_{0.35}TiO_3$ [145]	$LiMn_2O_4$	$Li_4Mn_5O_{12}$ (163 mAh g^{-1})	2.5 (2%,0.004 C)	
$Li_{0.35}La_{0.55}TiO_3$ [146]	$LiMn_2O_4$ (148)	Li	71 (48%, 0.01 C)	
$Li_{0.35}La_{0.55}TiO_3$ [147]	$LiMn_2O_4$ (148)	Li	27 (18%, 0.05 C)	~22 (5th)

LATP interface remained stable during cycling, which was superior to interfaces between $LiCoO_2$ and sulfide electrolytes.

For garnet-type electrolytes, ASSBs were constructed by sol-gel [141], screen-printing [142], atomic layer deposition (ALD) [143] et al. The cell consisted of $LiCoO_2/Li_7La_3Zr_2O_{12}/Li$ stacking showed large capacity loss during charge-discharge with an initial discharge capacity of only 0.2% of the theoretical one, probably due to high interfacial resistance between $LiCoO_2$ and $Li_7La_3Zr_2O_{12}$ [141]. The $LiCoO_2$/Nb-doped $Li_7La_3Zr_2O_{12}$/Li cell was prepared from screen-printing $LiCoO_2$ that was pre-mixed with Li_3BO_3 powder [142]. Since Li_3BO_3 has rather low melting temperature, $LiCoO_2$ could be fused well with the electrolyte. The initial discharge capacity was 74% of the theoretical one, and the coulombic efficiency was almost 100% from 2nd to 5th cycles. The electrochemical performance could be comparable to ASSB prepared by physical vapor deposition, which revealed that incorporation of Li_3BO_3 into cathode was beneficial for ASSB construction. Han et al. [143] constructed a $Li_2FeMn_3O_8/Li_7La_{2.75}Ca_{0.25}Zr_{1.75}Nb_{0.25}O_{12}$/ALD-$Al_2O_3$/Li ASSB. Al_2O_3 was deposited between Li and $Li_7La_{2.75}Ca_{0.25}Zr_{1.75}Nb_{0.25}O_{12}$ by atomic layer deposition (ALD), and some high-voltage liquid organic electrolyte was added between $Li_2FeMn_3O_8$ and $Li_7La_{2.75}Ca_{0.25}Zr_{1.75}Nb_{0.25}O_{12}$ to reduce interfacial resistances between the electrodes and the solid electrolyte. The initial discharge capacity was 70% of the theoretical one, and the capacity maintained at 110 mAh g^{-1} after 50 cycles. The promising performance of the ASSB was mainly due to the interface improvement. Wu et al. [49] fabricated a $LiFePO_4/Li_{6.20}Ga_{0.30}La_{2.95}Rb_{0.05}Zr_2O_{12}$/Li ASSB. Li$(CF_3SO_2)_2N$ electrolytic salt was added into cathode to reduce interfacial resistance. The initial discharge capacity at 60 °C was 88% of the theoretical one, and the capacity decreased to 110 mAh g^{-1} after 20 cycles, which was caused by unstable contact between the electrodes and the electrolyte. Luo et al. [144] constructed a $LiFePO_4$/gel electrolyte/$Li_7La_3Zr_2O_{12}$/Ge/Li ASSB. A gel membrane was placed between $LiFePO_4$ and $Li_7La_3Zr_2O_{12}$ to decrease interfacial resistance. A Ge layer was deposited between $Li_7La_3Zr_2O_{12}$ and Li by evaporation, which could alloy with Li and improve wetting at interface. The initial discharge capacity was 81% of the theoretical one, and the battery exhibited a high capacity of 140 mAh g^{-1} after 100 cycles, which was comparable to battery with liquid electrolyte.

Kotobuki et al. [145–147] fabricated several ASSBs based on perovskite-type electrolytes, which were honeycomb or 3 dimensionally ordered macroporous (3DOM) structured. For an ASSB $LiMn_2O_4$/honeycomb $Li_{0.55}La_{0.35}TiO_3/Li_4Mn_5O_{12}$, electrodes were prepared by impregnation of active materials and respective precursor sol into the honeycomb holes and followed by calcination [145]. The initial discharge capacity was only 2% of the theoretical one. To enhance performance of the ASSB, it requires improvement of electrode preparation and 3D structure of the solid electrolyte. A $Li_{0.35}La_{0.55}TiO_3$ electrolyte with a 3 dimensionally ordered microporous (3DOM) structured layer and a honeycomb layer was prepared by a colloidal crystal templating method and calcination, which was applied to an ASSB with $LiMn_2O_4$ and Li as cathode and anode [146]. The 3DOM structure could increase contact area between cathode and solid electrolyte. However, the ASSB only possessed an initial discharge capacity of 48% of the theoretical one, due mainly to low regularity of the porous structure and long Li-ion diffusion path in the honeycomb electrolyte. A 2-layered $Li_{0.35}La_{0.55}TiO_3$ with a 3 dimensionally ordered microporous (3DOM) layer and a dense layer was also fabricated by suspension filtration method [147]. The electrolyte was assembled into an ASSB with $LiMn_2O_4$ and Li as electrodes, which showed an initial discharge capacity of 18% of the theoretical one and maintained capacity of ~22 mAh g^{-1} after 5 cycles.

Summarized in Table 2, most of the ASSBs had lower capacities than their counterparts based on liquid electrolyte and short charge-discharge cycles of no more than 100. The ASSB $LiFePO_4$/gel electrolyte/$Li_7La_3Zr_2O_{12}$/Ge/Li showed excellent retention for 100 cycles [144], however, capacity fading may appear for longer cycles as in practical application. Interfacial resistance is the main obstacle limiting performance of ASSB. Many effective methods have been adopted to reduce interfacial resistance, as mentioned above, and further interface improvement is necessary to promote application of ASSB.

5. Conclusions

LISICON- and LiPON-type of solid electrolytes had low ionic conductivities, Li_3N-type of solid electrolytes had narrow electrochemical stability windows, sulfide-, argyrodite- and anti-perovskite-type solid electrolytes were not stable in the ambient atmosphere. NASICON-, garnet- and perovskite-type solid electrolytes are promising for applications in ASSBs. With careful selection of solid electrolytes, highly safe battery cells can be constructed. With improvement of interfaces, interfacial resistances can be reduced and ASSBs can show better performance. However, ASSBs still need to be encapsulated to avoid contamination from the ambient environment, which can result in decrease in ionic conductivity and change of structure. Further effort is needed to improve properties of solid electrolytes and compatibility between solid electrolytes and electrodes.

Acknowledgements

This research is supported by National University of Singapore, and National Natural Science Foundation of China through NSFC 51572182.

Feng Zheng would like to thank National University of Singapore for financial support.

References

[1] Y. Nishi, J. Power Sources 100 (2001) 101–106.
[2] M. Armand, J.-M. Tarascon, Nature 451 (2008) 652–657.
[3] W. Li, J.R. Dahn, D.S. Wainwright, Science 264 (1994) 1115–1118.
[4] B. Owens, P. Skarstad, Solid State Ionics 53 (1992) 665–672.
[5] X. Yao, B. Huang, J. Yin, G. Peng, Z. Huang, C. Gao, D. Liu, X. Xu, Chin. Phys. B 25 (2016) 018802.
[6] X. Xu, Z. Qiu, Y. Guan, Z. Huang, Y. Jin, Energy Storage Science and Technology 2 (2013) 331–341.
[7] C. Chen, S. Xie, E. Sperling, A. Yang, G. Henriksen, K. Amine, Solid State Ionics 167 (2004) 263–272.
[8] K. Takada, Acta Mater. 61 (2013) 759–770.
[9] J.C. Bachman, S. Muy, A. Grimaud, H.-H. Chang, N. Pour, S.F. Lux, O. Paschos, F. Maglia, S. Lupart, P. Lamp, L. Giordano, Y. Shao-Horn, Chem. Rev. 116 (2016) 140–162.
[10] B. Boukamp, R. Huggins, Phys. Lett. A 58 (1976) 231–233.
[11] Y. Zhao, L.L. Daemen, J. Am. Chem. Soc. 134 (2012) 15042–15047.
[12] L.O. Hagman, P. Kierkegaard, Acta Chem. Scand. 22 (1968) 1822–1832.
[13] H.-P. Hong, Mater. Res. Bull. 11 (1976) 173–182.
[14] L. Sebastian, J. Gopalakrishnan, J. Mater. Chem. 13 (2003) 433–441.
[15] J. Goodenough, H.-P. Hong, J. Kafalas, Mater. Res. Bull. 11 (1976) 203–220.
[16] F. Sudreau, D. Petit, J.P. Boilot, J. Solid State Chem. 83 (1989) 78–90.
[17] H. Aono, N. Imanaka, G.-y. Adachi, Acc. Chem. Res. 27 (1994) 265–270.
[18] H. Aono, E. Sugimoto, Y. Sadaoka, N. Imanaka, G.-y. Adachi, Solid State Ionics 47 (1991) 257–264.
[19] H. Aono, E. Sugimoto, Y. Sadaaka, N. Imanaka, G. Adachi, J. Electrochem. Soc. 136 (1989) 590.
[20] H. Aono, E. Sugimoto, Y. Sadaoka, N. Imanaka, G.-y. Adachi, J. Electrochem. Soc. 137 (1990) 1023–1027.
[21] H. Aono, E. Sugimoto, Y. Sadaoka, N. Imanaka, G.-y. Adachi, Solid State Ionics 40 (1990) 38–42.
[22] J. Fu, J. Am. Ceram. Soc. 80 (1997) 1901–1903.
[23] P. Goharian, B. Eftekhari Yekta, A.R. Aghaei, S. Banijamali, J. Non-Cryst. Solids 409 (2015) 120–125.
[24] H. Eckert, A.C. Martins Rodrigues, MRS Bull. 42 (2017) 206–212.
[25] Y. Ren, K. Chen, R. Chen, T. Liu, Y. Zhang, C.W. Nan, J. Am. Ceram. Soc. 98 (2015) 3603–3623.
[26] C. Delmas, A. Nadiri, J.L. Soubeyroux, Solid State Ionics 28 (1988) 419–423.
[27] A. Aatiq, M. Ménétrier, L. Croguennec, E. Suard, C. Delmas, J. Mater. Chem. 12 (2002) 2971–2978.
[28] J. Fu, Solid State Ionics 104 (1997) 191–194.
[29] X. Xu, Z. Wen, X. Wu, X. Yang, Z. Gu, J. Am. Ceram. Soc. 90 (2007) 2802–2806.
[30] J.S. Thokchom, N. Gupta, B. Kumar, J. Electrochem. Soc. 155 (2008) A915–A920.
[31] M. Illbeigi, A. Fazlali, M. Kazazi, A.H. Mohammadi, Solid State Ionics 289 (2016) 180–187.
[32] G.B. Kunshina, I.V. Bocharova, V.I. Ivanenko, Inorg. Mater.: Applied Research 8

(2017) 238–244.
[33] S.S. Berbano, J. Guo, H. Guo, M.T. Lanagan, C.A. Randall, J. Am. Ceram. Soc. 100 (2017) 2123–2135.
[34] J.K. Feng, L. Lu, M.O. Lai, J. Alloy. Comp. 501 (2010) 255–258.
[35] E. Zhao, F. Ma, Y. Guo, Y. Jin, RSC Adv. 6 (2016) 92579–92585.
[36] H.M. Kasper, lnorg. Chem. 8 (1969) 1000–1002.
[37] V. Thangadurai, H. Kaack, W.J. Weppner, J. Am. Ceram. Soc. 86 (2003) 437–440.
[38] V. Thangadurai, W. Weppner, Adv. Funct. Mater. 15 (2005) 107–112.
[39] E.J. Cussen, Chem. Commun. (2006) 412–413.
[40] R. Murugan, V. Thangadurai, W. Weppner, Angew. Chem. Int. Ed. 46 (2007) 7778–7781.
[41] C.A. Geiger, E. Alekseev, B. Lazic, M. Fisch, T. Armbruster, R. Langner, M. Fechtelkord, N. Kim, T. Pettke, W. Weppner, lnorg. Chem. 50 (2010) 1089–1097.
[42] S. Ohta, T. Kobayashi, T. Asaoka, J. Power Sources 196 (2011) 3342–3345.
[43] R. Murugan, S. Ramakumar, N. Janani, Electrochem. Commun. 13 (2011) 1373–1375.
[44] Y. Li, J.-T. Han, C.-A. Wang, H. Xie, J.B. Goodenough, J. Mater. Chem. 22 (2012) 15357–15361.
[45] C. Bernuy-Lopez, W. Manalastas, J.M. Lopez del Amo, A. Aguadero, F. Aguesse, J.A. Kilner, Chem. Mater. 26 (2014) 3610–3617.
[46] D. Rettenwander, G.n. Redhammer, F. Preishuber-Pflügl, L. Cheng, L. Miara, R. Wagner, A. Welzl, E. Suard, M.M. Doeff, M. Wilkening, Chem. Mater. 28 (2016) 2384–2392.
[47] J.-F. Wu, E.-Y. Chen, Y. Yu, L. Liu, Y. Wu, W.K. Pang, V.K. Peterson, X. Guo, ACS Appl. Mater. Interfaces 9 (2017) 1542–1552.
[48] L. Buannic, B. Orayech, J.-M. López Del Amo, J. Carrasco, N.A. Katcho, F.d.r. Aguesse, W. Manalastas, W. Zhang, J. Kilner, A. Llordés, Chem. Mater. 29 (2017) 1769–1778.
[49] J.F. Wu, W.K. Pang, V.K. Peterson, L. Wei, X. Guo, ACS Appl. Mater. Interfaces 9 (2017) 12461–12468.
[50] G. Larraz, A. Orera, M. Sanjuan, J. Mater. Chem. A 1 (2013) 11419–11428.
[51] W. Xia, B. Xu, H. Duan, X. Tang, Y. Guo, H. Kang, H. Li, H. Liu, J. Am. Ceram. Soc. 100 (2017) 2832–2839.
[52] Y. Inaguma, C. Liquan, M. Itoh, T. Nakamura, T. Uchida, H. Ikuta, M. Wakihara, Solid State Commun. 86 (1993) 689–693.
[53] S. Stramare, V. Thangadurai, W. Weppner, Chem. Mater. 15 (2003) 3974–3990.
[54] Y. Inaguma, L. Chen, M. Itoh, T. Nakamura, Solid State Ionics 70 (1994) 196–202.
[55] C. Chen, K. Amine, Solid State Ionics 144 (2001) 51–57.
[56] H.-T. Chung, J.-G. Kim, H.-G. Kim, Solid State Ionics 107 (1998) 153–160.
[57] V. Thangadurai, A. Shukla, J. Gopalakrishnan, Chem. Mater. 11 (1999) 835–839.
[58] R. Inada, K. Kimura, K. Kusakabe, T. Tojo, Y. Sakurai, Solid State Ionics 261 (2014) 95–99.
[59] K. Kimura, K. Wagatsuma, T. Tojo, R. Inada, Y. Sakurai, Ceram. Int. 42 (2016) 5546–5552.
[60] B. Huang, B. Xu, Y. Li, W. Zhou, Y. You, S. Zhong, C.A. Wang, J.B. Goodenough, ACS Appl. Mater. Interfaces 8 (2016) 14552–14557.
[61] R. Yu, Q.-X. Du, B.-K. Zou, Z.-Y. Wen, C.-H. Chen, J. Power Sources 306 (2016) 623–629.
[62] Y. Kong, Y. Li, J. Lu, Ceram. Int. 43 (2017) 5642–5646.
[63] J. Lu, Y. Li, Y. Kong, N. Zhang, Ceram. Int. 44 (5) (2017) 4744–4750.
[64] Y. Li, W. Zhou, X. Chen, X. Lü, Z. Cui, S. Xin, L. Xue, Q. Jia, J.B. Goodenough, Proc. Natl. Acad. Sci. U.S.A. 113 (2016) 13313–13317.
[65] H.-P. Hong, Mater. Res. Bull. 13 (1978) 117–124.
[66] U.v. Alpen, M.F. Bell, W. Wichelhaus, K.Y. Cheung, G.J. Dudley, Electrochim. Acta 23 (1978) 1395–1397.
[67] D. Mazumdar, D.N. Bose, M.L. Mukherjee, Solid State Ionics 14 (1984) 143–147.
[68] Y.A. Du, N. Holzwarth, J. Electrochem. Soc. 154 (2007) A999–A1004.
[69] J. Kuwano, A.R. West, Mater. Res. Bull. 15 (1980) 1661–1667.
[70] Y.W. Hu, I.D. Raistrick, R.A. Huggins, J. Electrochem. Soc. 124 (1977) 1240–1242.
[71] S. Song, J. Lu, F. Zheng, H.M. Duong, L. Lu, RSC Adv. 5 (2015) 6588–6594.
[72] Y. Deng, C. Eames, B. Fleutot, R.n. David, J.-N.l. Chotard, E. Suard, C. Masquelier, M.S. Islam, ACS Appl. Mater. Interfaces 9 (2017) 7050–7058.
[73] N. Kamaya, K. Homma, Y. Yamakawa, M. Hirayama, R. Kanno, M. Yonemura, T. Kamiyama, Y. Kato, S. Hama, K. Kawamoto, Nat. Mater. 10 (2011) 682–686.
[74] J. Bates, N. Dudney, G. Gruzalski, R. Zuhr, A. Choudhury, C. Luck, J. Robertson, J. Power Sources 43 (1993) 103–110.
[75] N. Suzuki, T. Inaba, T. Shiga, Thin Solid Films 520 (2012) 1821–1825.
[76] G. Li, M. Li, L. Dong, X. Li, D. Li, Int J. Hydrogen Energy 39 (2014) 17466–17472.
[77] Y. Su, J. Falgenhauer, A. Polity, T. Leichtweiß, A. Kronenberger, J. Obel, S. Zhou, D. Schlettwein, J. Janek, B.K. Meyer, Solid State Ionics 282 (2015) 63–69.
[78] T. Fujibayashi, Y. Kubota, K. Iwabuchi, N. Yoshii, AIP Adv. 7 (2017).
[79] L. Le Van-Jodin, A. Claudel, C. Secouard, F. Sabary, J.-P. Barnes, S. Martin, Electrochim. Acta 259 (2018) 742–751.
[80] Y. Hamon, A. Douard, F. Sabary, C. Marcel, P. Vinatier, B. Pecquenard, A. Levasseur, Solid State Ionics 177 (2006) 257–261.
[81] B. Wang, J. Bates, F. Hart, B. Sales, R. Zuhr, J. Robertson, J. Electrochem. Soc. 143 (1996) 3203–3213.
[82] N. Dudney, B. Neudecker, Curr. Opin. Solid State Mater. Sci. 4 (1999) 479–482.
[83] X. Yu, J. Bates, G. Jellison, F. Hart, J. Electrochem. Soc. 144 (1997) 524–532.
[84] R.A. Huggins, Electrochim. Acta 22 (1977) 773–781.
[85] J.R. Rea, D.L. Foster, P.R. Mallory, I. Co, Mater. Res. Bull. 14 (1979) 841–846.
[86] P. Hartwig, W. Weppner, W. Wichelhaus, A. Rabenau, Angew. Chem. Int. Ed. 19 (1980) 74–75.
[87] W. Weppner, P. Hartwig, A. Rabenau, J. Power Sources 6 (1981) 251–259.
[88] K. Kitahama, Y. Furukawa, S. Kawai, O. Nakamura, Solid State Ionics 3–4 (1981) 335–339.
[89] S. Hatake, J. Kuwano, M. Miyamori, Y. Saito, S. Koyama, J. Power Sources 68 (1997) 416–420.
[90] H. Yamane, S. Kikkawa, M. Koizumi, Solid State Ionics 15 (1985) 51–54.
[91] E. Narimatsu, Y. Yamamoto, T. Nishimura, N. Hirosaki, J. Ceram. Soc. Jpn. 118 (2010) 837–841.
[92] E. Narimatsu, Y. Yamamoto, T. Takeda, T. Nishimura, N. Hirosaki, J. Mater. Res. 26 (2011) 1133–1142.
[93] M. Tatsumisago, A. Hayashi, Int. J. Appl. Glass Sci. 5 (2014) 226–235.
[94] R. Kanno, M. Murayama, J. Electrochem. Soc. 148 (2001) A742–A746.
[95] R. Kanno, T. Hata, Y. Kawamoto, M. Irie, Solid State Ionics 130 (2000) 97–104.
[96] Y. Mo, S.P. Ong, G. Ceder, Chem. Mater. 24 (2011) 15–17.
[97] S.P. Ong, Y. Mo, W.D. Richards, L. Miara, H.S. Lee, G. Ceder, Energy Environ. Sci. 6 (2013) 148–156.
[98] Y. Sun, K. Suzuki, K. Hara, S. Hori, T.A. Yano, M. Hara, M. Hirayama, R. Kanno, J. Power Sources 324 (2016) 798–803.
[99] Y. Kato, S. Hori, T. Saito, K. Suzuki, M. Hirayama, A. Mitsui, M. Yonemura, H. Iba, R. Kanno, Nature Energy 1 (2016) 16030.
[100] W.D. Richards, Y. Wang, L.J. Miara, J.C. Kim, G. Ceder, Energy Environ. Sci. 9 (2016) 3272–3278.
[101] A. Kulkarni, H. Maiti, A. Paul, Bull. Mater. Sci. 6 (1984) 201–221.
[102] F. Mizuno, A. Hayashi, K. Tadanaga, M. Tatsumisago, Adv. Mater. 17 (2005) 918–921.
[103] Z. Zhang, J.H. Kennedy, Solid State Ionics 38 (1990) 217–224.
[104] A. Hayashi, S. Hama, H. Morimoto, M. Tatsumisago, T. Minami, J. Am. Ceram. Soc. 84 (2001) 477–479.
[105] T. Minami, N. Machida, Mat. Sci. Eng. B-Solid 13 (1992) 203–208.
[106] A. Hayashi, S. Hama, H. Morimoto, M. Tatsumisago, T. Minami, Chem. Lett. 30 (2001) 872–873.
[107] M. Tatsumisago, S. Hama, A. Hayashi, H. Morimoto, T. Minami, Solid State Ionics 154 (2002) 635–640.
[108] M. Tachez, J.-P. Malugani, R. Mercier, G. Robert, Solid State Ionics 14 (1984) 181–185.
[109] A. Hayashi, S. Hama, T. Minami, M. Tatsumisago, Electrochem. Commun. 5 (2003) 111–114.
[110] F. Mizuno, A. Hayashi, K. Tadanaga, M. Tatsumisago, Solid State Ionics 177 (2006) 2721–2725.
[111] H. Yamane, M. Shibata, Y. Shimane, T. Junke, Y. Seino, S. Adams, K. Minami, A. Hayashi, M. Tatsumisago, Solid State Ionics 178 (2007) 1163–1167.
[112] K. Minami, F. Mizuno, A. Hayashi, M. Tatsumisago, Solid State Ionics 178 (2007) 837–841.
[113] Y. Seino, T. Ota, K. Takada, A. Hayashi, M. Tatsumisago, Energy Environ. Sci. 7 (2014) 627–631.
[114] I.H. Chu, H. Nguyen, S. Hy, Y.C. Lin, Z. Wang, Z. Xu, Z. Deng, Y.S. Meng, S.P. Ong, ACS Appl. Mater. Interfaces 8 (2016) 7843–7853.
[115] H. Muramatsu, A. Hayashi, T. Ohtomo, S. Hama, M. Tatsumisago, Solid State Ionics 182 (2011) 116–119.
[116] H.J. Deiseroth, S.T. Kong, H. Eckert, J. Vannahme, C. Reiner, T. Zaiß, M. Schlosser, Angew. Chem. Int. Ed. 47 (2008) 755–758.
[117] O. Pecher, S.T. Kong, T. Goebel, V. Nickel, K. Weichert, C. Reiner, H.J. Deiseroth, J. Maier, F. Haarmann, D. Zahn, Chem. Eur J. 16 (2010) 8347–8354.
[118] V. Epp, O.z.l. Gün, H.-J.r. Deiseroth, M. Wilkening, J. Phys. Chem. Lett. 4 (2013) 2118–2123.
[119] S. Boulineau, M. Courty, J.-M. Tarascon, V. Viallet, Solid State Ionics 221 (2012) 1–5.
[120] R.P. Rao, S. Adams, Phys. Status Solidi A 208 (2011) 1804–1807.
[121] P.R. Rayavarapu, N. Sharma, V.K. Peterson, S. Adams, J. Solid State Electrochem. 16 (2012) 1807–1813.
[122] R.P. Rao, N. Sharma, V. Peterson, S. Adams, Solid State Ionics 230 (2013) 72–76.
[123] M. Chen, R.P. Rao, S. Adams, Solid State Ionics 262 (2014) 183–187.
[124] M. Chen, R.P. Rao, S. Adams, Solid State Ionics 268 (2014) 300–304.
[125] M. Chen, S. Adams, J. Solid State Electrochem. 19 (2015) 697–702.
[126] M. Chen, X. Yin, M. Reddy, S. Adams, J. Mater. Chem. A 3 (2015) 10698–10702.
[127] C. Yu, L. van Eijck, S. Ganapathy, M. Wagemaker, Electrochim. Acta 215 (2016) 93–99.
[128] Z. Zhang, L. Zhang, Y. Liu, C. Yu, X. Yan, B. Xu, L.M. Wang, J. Alloy. Comp. 747 (2018) 227–235.
[129] H. Schneider, H. Du, T. Kelley, K. Leitner, J. ter Maat, C. Scordilis-Kelley, R. Sanchez-Carrera, I. Kovalev, A. Mudalige, J. Kulisch, M.M. Safont-Sempere, P. Hartmann, T. Weiβ, L. Schneider, B. Hinrichsen, J. Power Sources 366 (2017) 151–160.
[130] A. Emly, E. Kioupakis, A. Van der Ven, Chem. Mater. 25 (2013) 4663–4670.
[131] Y. Zhang, Y. Zhao, C. Chen, Phys. Rev. B 87 (2013) 134303.
[132] Z. Deng, B. Radhakrishnan, S.P. Ong, Chem. Mater. 27 (2015) 3749–3755.
[133] M. Braga, J.A. Ferreira, V. Stockhausen, J. Oliveira, A. El-Azab, J. Mater. Chem. A 2 (2014) 5470–5480.
[134] H. Fang, S. Wang, J. Liu, Q. Sun, P. Jena, J. Mater. Chem. A 5 (2017) 13373–13381.
[135] H. Fang, P. Jena, Proc. Natl. Acad. Sci. U. S. A 114 (2017) 11046–11051.
[136] X. Lü, J.W. Howard, A. Chen, J. Zhu, S. Li, G. Wu, P. Dowden, H. Xu, Y. Zhao, Q. Jia, Adv. Sci. 3 (2016) 1500359.
[137] Y.H. Rho, K. Kanamura, J. Power Sources 158 (2006) 1436–1441.
[138] K. Dokko, K. Hoshina, H. Nakano, K. Kanamura, J. Power Sources 174 (2007) 1100–1103.
[139] E. Kobayashi, L.S. Plashnitsa, T. Doi, S. Okada, J.-i. Yamaki, Electrochem. Commun. 12 (2010) 894–896.

[140] H.-S. Kim, Y. Oh, K.H. Kang, J.H. Kim, J. Kim, C.S. Yoon, ACS Appl. Mater. Interfaces 9 (2017) 16063–16070.
[141] M. Kotobuki, H. Munakata, K. Kanamura, Y. Sato, T. Yoshida, J. Electrochem. Soc. 157 (2010) A1076–A1079.
[142] S. Ohta, S. Komagata, J. Seki, T. Saeki, S. Morishita, T. Asaoka, J. Power Sources 238 (2013) 53–56.
[143] X. Han, Y. Gong, K.K. Fu, X. He, G.T. Hitz, J. Dai, A. Pearse, B. Liu, H. Wang, G. Rubloff, Nat. Mater. 16 (2017) 572.
[144] W. Luo, Y. Gong, Y. Zhu, Y. Li, Y. Yao, Y. Zhang, K.K. Fu, G. Pastel, C.F. Lin, Y. Mo, Adv. Mater. 29 (2017).
[145] M. Kotobuki, Y. Suzuki, H. Munakata, K. Kanamura, Y. Sato, K. Yamamoto, T. Yoshida, Electrochim. Acta 56 (2011) 1023–1029.
[146] M. Kotobuki, Y. Suzuki, K. Kanamura, Y. Sato, K. Yamamoto, T. Yoshida, J. Power Sources 196 (2011) 9815–9819.
[147] M. Kotobuki, R. Osone, H. Munakata, K. Kanamura, Energy Harvesting and Storage: Materials, Devices, and Applications II, International Society for Optics and Photonics, 2011, p. 80350C.